

University of Groningen

The LOFAR EoR Data Model

Labropoulos, P.; Koopmans, L. V. E.; Jelić, V.; Pandey, V. N.; Schaye, J.; Zaroubi, S.

Published in:
 ArXiv

IMPORTANT NOTE: You are advised to consult the publisher's version (publisher's PDF) if you wish to cite from it. Please check the document version below.

Document Version
 Publisher's PDF, also known as Version of record

Publication date:
 2009

[Link to publication in University of Groningen/UMCG research database](#)

Citation for published version (APA):

Labropoulos, P., Koopmans, L. V. E., Jelić, V., Pandey, V. N., Schaye, J., & Zaroubi, S. (2009). The LOFAR EoR Data Model: (I) Effects of Noise and Instrumental Corruptions on the 21-cm Reionization Signal-Extraction Strategy. *ArXiv*.

Copyright

Other than for strictly personal use, it is not permitted to download or to forward/distribute the text or part of it without the consent of the author(s) and/or copyright holder(s), unless the work is under an open content license (like Creative Commons).

The publication may also be distributed here under the terms of Article 25fa of the Dutch Copyright Act, indicated by the "Taverne" license. More information can be found on the University of Groningen website: <https://www.rug.nl/library/open-access/self-archiving-pure/taverne-amendment>.

Take-down policy

If you believe that this document breaches copyright please contact us providing details, and we will remove access to the work immediately and investigate your claim.

Downloaded from the University of Groningen/UMCG research database (Pure): <http://www.rug.nl/research/portal>. For technical reasons the number of authors shown on this cover page is limited to 10 maximum.

The LOFAR EoR Data Model: (I) Effects of Noise and Instrumental Corruptions on the 21-cm Reionization Signal-Extraction Strategy

P. Labropoulos^{1*}, L. V. E. Koopmans¹, V. Jelić¹, S. Yatawatta¹, R. M. Thomas¹,
G. Bernardi¹, M. Brentjens², A.G. de Bruyn^{1,2}, B. Ciardi³, G. Harker¹, A.R. Offringa¹,
V. N. Pandey¹, J. Schaye⁴, S. Zaroubi¹

¹*Kapteyn Astronomical Institute, University of Groningen, P.O. Box 800, 9700 AV Groningen, the Netherlands*

²*ASTRON, Postbus 2, 7990 AA Dwingeloo, the Netherlands*

³*Max-Planck Institute for Astrophysics, Karl-Schwarzschild-Straße 1, 85748 Garching, Germany*

⁴*Leiden Observatory, Leiden University, PO Box 9513, 2300 RA Leiden, the Netherlands*

21 January 2009

ABSTRACT

A number of experiments are set to measure the 21-cm signal of neutral hydrogen from the Epoch of Reionization (EoR). The common denominator of these experiments are the large data sets produced, contaminated by various instrumental effects, ionospheric distortions, RFI and strong Galactic and extragalactic foregrounds. In this paper, the first in a series, we present the *Data Model* that will be the basis of the signal analysis for the LOFAR (Low Frequency Array) EoR Key Science Project (LOFAR EoR KSP). Using this data model we simulate realistic visibility data sets over a wide frequency band, taking properly into account all currently known instrumental corruptions (e.g. direction-dependent gains, complex gains, polarization effects, noise, etc). We then apply primary calibration errors to the data in a statistical sense, assuming that the calibration errors are random Gaussian variates at a level consistent with our current knowledge based on observations with the LOFAR Core Station 1. Our aim is to demonstrate how the systematics of an interferometric measurement affect the quality of the calibrated data, how errors correlate and propagate, and in the long run how this can lead to new calibration strategies. We present results of these simulations and the inversion process and extraction procedure. We also discuss some general properties of the coherency matrix and Jones formalism that might prove useful in solving the calibration problem of aperture synthesis arrays. We conclude that even in the presence of realistic noise and instrumental errors, the statistical signature of the EoR signal can be detected by LOFAR with relatively small errors. A detailed study of the statistical properties of our data model and more complex instrumental models will be considered in the future.

Key words: telescopes - techniques: interferometric - techniques: polarimetric - cosmology: observations - methods: statistical - methods: data analysis

1 INTRODUCTION

Recent years have seen a marked increase in the study, both theoretical and observational, of the epoch in the history of our Universe after the cosmological recombination era: from the so called ‘Dark Ages’ to the *Epoch of Reionization* (EoR) (Hogan & Rees 1979; Scott & Rees 1990; Madau, Meiksin, & Rees 1997). A cold and dark Universe, after the recombination era, was illuminated by sources of radiation, be it stars, quasars or dark matter annihilation. These ‘first objects’ ionized and heated their surrounding inter-

galactic medium (IGM), carving out ‘bubbles’ in the otherwise neutral hydrogen-filled Universe. These bubbles grew rapidly, both in size and number, and caused a phase transition in the hydrogen-ionized fraction of our Universe at redshifts $6 < z < 20$ (Sunyaev & Zeldovich 1975). Although the EoR spanned a relatively small fraction, in time, of the Universe’s age, its impact on subsequent structure formation (at least baryonic) is crucial. Hence, studying the EoR directly influences our understanding of issues in contemporary astrophysical research such as metal-poor stars, early galaxy formation, quasars and cosmology (Nusser 2005; Zaroubi & Silk 2005; Kuhlen & Madau 2005; Thomas & Zaroubi 2008; Field 1958, 1959; Scott & Rees 1990; Kumar, Subramanian, & Padman-

* E-mail: panos@astro.rug.nl

abhan 1995; Madau, Meiksin, & Rees 1997). For a detailed review of the EoR and our current efforts to detect it, we refer the reader to Furlanetto, Oh, & Briggs (2006) and the references therein.

Given the recent progress in developing a concrete theoretical framework, and simulations based thereon, the EoR from an observational point of view is still very poorly constrained. Despite a wealth of observational cosmological data made available during the past years (e.g. Spergel et al. 2007; Page et al. 2007; Becker et al. 2001; Fan et al. 2001; Pentericci et al. 2002; White et al. 2003; Fan et al. 2006), data directly probing the EoR have eluded scientists and the ones that constrain the EoR are indirect and very model-dependent (Barkana & Loeb 2001; Loeb & Barkana 2001; Ciardi, Ferrara, & White 2003; Ciardi, Stoehr, & White 2003; Bromm & Larson 2004; Iliiev et al. 2007; Zaroubi et al. 2007; Thomas & Zaroubi 2008). Currently there are two main observational constraints on the EoR: first, the sudden jump in the Lyman- α optical depth in the Gunn–Peterson troughs (Gunn & Peterson 1965), observed in the quasar spectra of the Sloan Digital Sky Survey (SDSS) (Becker et al. 2001; Fan et al. 2001; Pentericci et al. 2002; White et al. 2003; Fan et al. 2006) which provides a limit on when reionization was completed. Current consensus is that reionization ended around a redshift of six. Second, the five-year *WMAP* data on the temperature and polarization anisotropies of the cosmic microwave background (CMB) (Spergel et al. 2007; Page et al. 2007) which gives an integral constraint on the Thomson optical depth for scattering experienced by the CMB photons since the EoR. A maximum likelihood analysis performed by Spergel et al. (2007) estimates the peak of reionization to have occurred at 11.3 when the cosmic age was 365 Myr. Thus, we see that current astronomical data is only able to provide us with crude boundaries within which reionization occurred. In order to properly characterize the onset, evolution and completion of the EoR and derive results on its impact on subsequent evolution of structures in the Universe, we need more direct measurements from the EoR.

Observations of the hydrogen 21-cm hyperfine “spin-flip” transition, using radio interferometry, provide just such a direct probe of the dark ages and the EoR over a wide spatial and redshift range. It is worth mentioning that the “spatial range” here implies the two dimensions on the sky, which is a function of the baseline lengths of an interferometer, and the third dimension along the redshift direction, which depends on the frequency resolution of the observation. The 21-cm emission line from the EoR is redshifted by $1+z$, because of the expansion of the Universe, to wavelengths in the meter waveband. For example, at a redshift of $z = 9$ the 21-cm line is redshifted to 2.1 metres, which corresponds to a frequency of about 140 MHz. Computer simulations suggest that we may expect a complex, evolving patch-work of neutral (H_I) and ionized hydrogen (H_{II}) regions. If we manage to successfully image the Universe at these high redshifts ($6 < z < 12$) we expect to find H_{II} regions, created by ionizing radiation from first objects, to appear as “holes” in an otherwise neutral hydrogen-filled Universe; the so-called *Swiss-cheese model*. Current constraints and simulations converge on reionization happening for a large part in the redshift range $z \approx 11.4$ (~ 115 MHz) to $z \approx 6$ (~ 203 MHz), which is the range probed by LOFAR¹, a radio interferometer currently being built near the village of Exloo in the Netherlands. The 21-cm radiation can not only trace the matter power spectrum in the period after recombination, but also can constrain reionization scenarios (Thomas & Zaroubi 2008; Barkana & Loeb 2001). Note that

because strongly radiating sources create bubbles of ionized gas inside the neutral IGM, one should observe fluctuations in the 21-cm emission due to reionization that deviate from those of neutral gas tracing the dark-matter distribution, even deep into the highly linear regime.

Developments in radio-wave sensor technologies in recent years have enabled us to conceive of and design extremely large, high sensitivity and high resolution radio interferometers, a development which is essential to conduct a successful 21-cm experiment to image the EoR. A series of radio telescopes are being built similar to LOFAR, such as MWA², PAPER³, 21CMA⁴ and further in the future the SKA⁵, all with one of their primary goals being the detection of the redshifted 21-cm signal from the EoR. The GMRT⁶ has a programme already under way to detect the EoR or at least to constrain the foregrounds that may hamper the experiment (Pen et al. 2008).

Calculations predict the cosmological 21-cm signal from the EoR to be extremely faint. Apart from the intrinsic low strength of the 21-cm signal, the experiment is plagued by a myriad of signal contaminants like man-made and natural (e.g. lightnings) interference, ionospheric distortions, Galactic free-free and synchrotron radiation, clusters and radio galaxies along the path of the signal. Thus long integration times, exquisite calibration and well-designed RFI mitigation techniques are needed in order to ensure the detection of the underlying signal. It is also imperative to properly model all these effects beforehand, in order to develop sophisticated schemes that will be needed to clean the data cubes from these contaminants (Shaver et al. 1999; Di Matteo, Ciardi, & Miniati 2004; Di Matteo et al. 2002; Oh & Mack 2003; Cooray & Furlanetto 2004; Zaldarriaga, Furlanetto, & Hernquist 2004; Gleser, Nusser, & Benson 2007). Due to the low signal-to-noise ratio per resolution element (of the order of 0.2 or for LOFAR and even less for e.g. MWA), the initial aim of all current experiments is to obtain a statistical detection of the signal. By statistical, we mean a global change in a property of the signal, for example the variance, as a function of frequency and angular scale. Note that this task involves distinguishing these statistical properties from those of the calibration residuals and the thermal noise.

In addition to the above-mentioned astrophysical and terrestrial sources of contamination, one also has to face issues arising in standard synthesis imaging. For that it is crucial to describe all physical effects on the signal that determine the values of the measured visibilities. The study of polarized radiation falls within the regime of optics: Hamaker & Bregman (1996) provided such a unifying model for the Jones and Mueller calculi in optics (Born & Wolf 1999) and the techniques of radio interferometry based on multiplying correlators. Because low frequency phased-array dipole antennas are inherently polarized, one has to consider polarimetry from the beginning. The Measurement Equation (ME) of Hamaker & Bregman (1996) is therefore a natural way to describe LOFAR. Their treatment (Hamaker & Bregman 1996; Sault, Hamaker, & Bregman 1996; Hamaker 2000c, 2006) forms the basis of our data model description and we will present it in a wider setting, giving the connection to physics. The Hamaker–Bregman–Sault measurement equation acts on the astronomical signals as

² Murchison Widefield Array: <http://www.haystack.mit.edu/ast/arrays/mwa>

³ Precision Array to Probe Epoch of Reionization: <http://astro.berkeley.edu/dbacker/eor/>

⁴ 21-cm Array: <http://web.phys.cmu.edu/past/>

⁵ Square Kilometer Array: <http://www.skatelescope.org>

⁶ Giant Meterwave Radio Telescope: <http://www.gmrt.ncra.tifr.res.in>

¹ Low Frequency Array: <http://www.lofar.org>

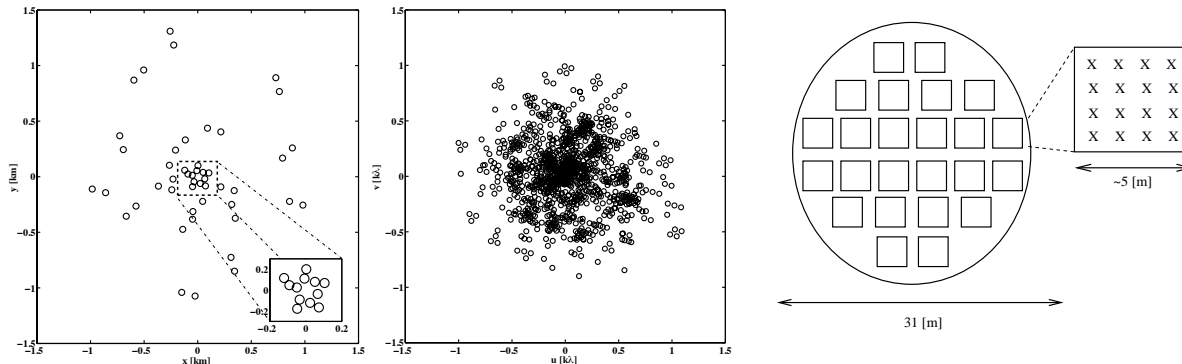


Figure 1. *Left:* The LOFAR compact-core layout situated near Exloo in the Netherlands. The open circle-size corresponds to the High Band Antenna (HBA) station size of approximately 31 metres in diameter. The 6 inner stations (“six-pack”) are shown in the the inset figure. *Middle:* The snapshot uv-coverage of the LOFAR compact core at the zenith and at a frequency 150 MHz. *Right:* The layout of a LOFAR HBA station. Each square represents a tile that consists of four by four, orthogonal bowtie dipoles, as shown in the blown-up inset. Each dipole pair can be rotated individually during the installation of the tile.

a “black-box”: the interferometer converts the input signal Stokes vectors to the final output at the correlator. This is done via a sequence of linear transformations and thus enables us to systematically model the series of effects that modify the signal while it propagates through the ionosphere and the receivers.

Calibration (Morales & Matejek 2008) of the observed visibility data set is generally aimed at determining instrumental parameters of the antennas at a level sufficient to detect signals at several times the noise level. While this is the traditional approach, a much more thorough understanding of the instrumental response is required in currently designed experiments such as the LOFAR EoR Key-Science Project, where unprecedented high dynamic range and sensitivity have to be achieved, and the signal is far below the noise level. For example, the CLEAN algorithm and variations on it have been used extensively, as an integral part of the SELFCAL process (Pearson & Readhead 1984). While computationally efficient, it does not provide a statistically optimal solution (Schwarz 1978; Starck, Pantin, & Murtagh 2002). In this work we shall therefore consider a maximum-likelihood solution to the measurement equation inversion problem (Boonstra 2005; Leshem, van der Veen, & Boonstra 2000; Leshem & van der Veen 2000; Wijnholds, Bregman, & Boonstra 2004), which takes into account realistic zero-mean calibration residuals and noise. We are also examining alternative solutions (Yatawatta et al. 2008), however.

After giving a short description of the LOFAR array, with emphasis on the high band (HBA) aspects of the design in Section 2, we review the basic relation between the observed visibilities and the sky intensity in section 3. We emphasize the polarized, matrix formulation of the measurement equation and the mathematical aspects of coherency matrix (Hamaker & Bregman 1996). In Section 4 we briefly discuss the relevant Measurement Equation (ME) parameters for LOFAR. Using this measurement equation as our data model, in Section 5, we produce a number of simulations for different instrumental parameters. This is the forward use of the data model. We also try to invert the data model, given the instrumental parameters and their error distributions, in order to recover the original data. Our goal is to test the calibration and inversion requirements using realistically generated data cubes. In Section 6 we discuss the results and give our conclusions.

2 DESCRIPTION OF THE LOW-FREQUENCY ARRAY

The immediate science goals of the LOFAR EoR-KSP, that drive some of the considerations about the design of LOFAR (Bregman 2002), are: (1) extract the 21-cm neutral hydrogen signal averaged along lines of sight, i.e. the ‘global signal’ (e.g. Shaver et al. 1999; Jelic et al. 2008), (2) determine the spatial-frequency power spectrum of the brightness temperature fluctuations on angular scales of about 1 arcminute to 1 degree and frequency scales between 0.1 and 10 MHz in the redshift range of ~ 6 -11 and (3) search for Strömgren ionization bubbles around bright sources and the 21-cm absorption-line forest (de Bruyn et al. 2007). In order to achieve these science goals, LOFAR requires a good uv-coverage, a good frequency coverage and a large collecting area.

Below, we give a short summary of the aspects of LOFAR which are relevant to the EoR experiment and our data model. For more details we refer to the project paper by de Bruyn et al. (in preparation).

2.1 Station configuration and uv-coverage

In its current layout, the LOFAR telescope (de Bruyn et al. 2007; Falcke et al. 2007) will consist of up to 48 stations of which approximately 24 will be located in the core region (Figure 1), near the village of Exloo in the Netherlands. The core marks an area of 1.7 by 2.3 kilometres. Each High Band Antenna station (HBA station; 110–240 MHz; see next section) in the core is further split into two “half-stations” of half the collecting area (~ 31 metre diameter), separated by ~ 130 metres. This split further improves the uv-coverage, though at the cost of quadrupling the BlueGene/P correlator demands (i.e. there are four times more base-lines). The central region of the core consists of six closely-packed stations, “the six-pack”, to ensure improved coverage of the shortest baselines necessary to map out the largest scales on the sky, such as the Milky Way. The station-layout yields a snapshot uv-coverage at the zenith as shown in Figure 1. The uv-coverages for a typical synthesis time of 4 hrs are shown in Figure 2.

A good uv-coverage is crucial for several reasons. First to improve sampling of the power spectrum of the EoR signal (Santos, Cooray, & Knox 2005; Hobson & Maisinger 2002; Bowman, Morales, & Hewitt 2008, 2006, 2005; Morales, Bowman, & Hewitt 2005). Second, to obtain precise Local (Nijboer, Noordam, & Yatawatta 2006) and Global (Smirnov & Noordam 2004) Sky mod-

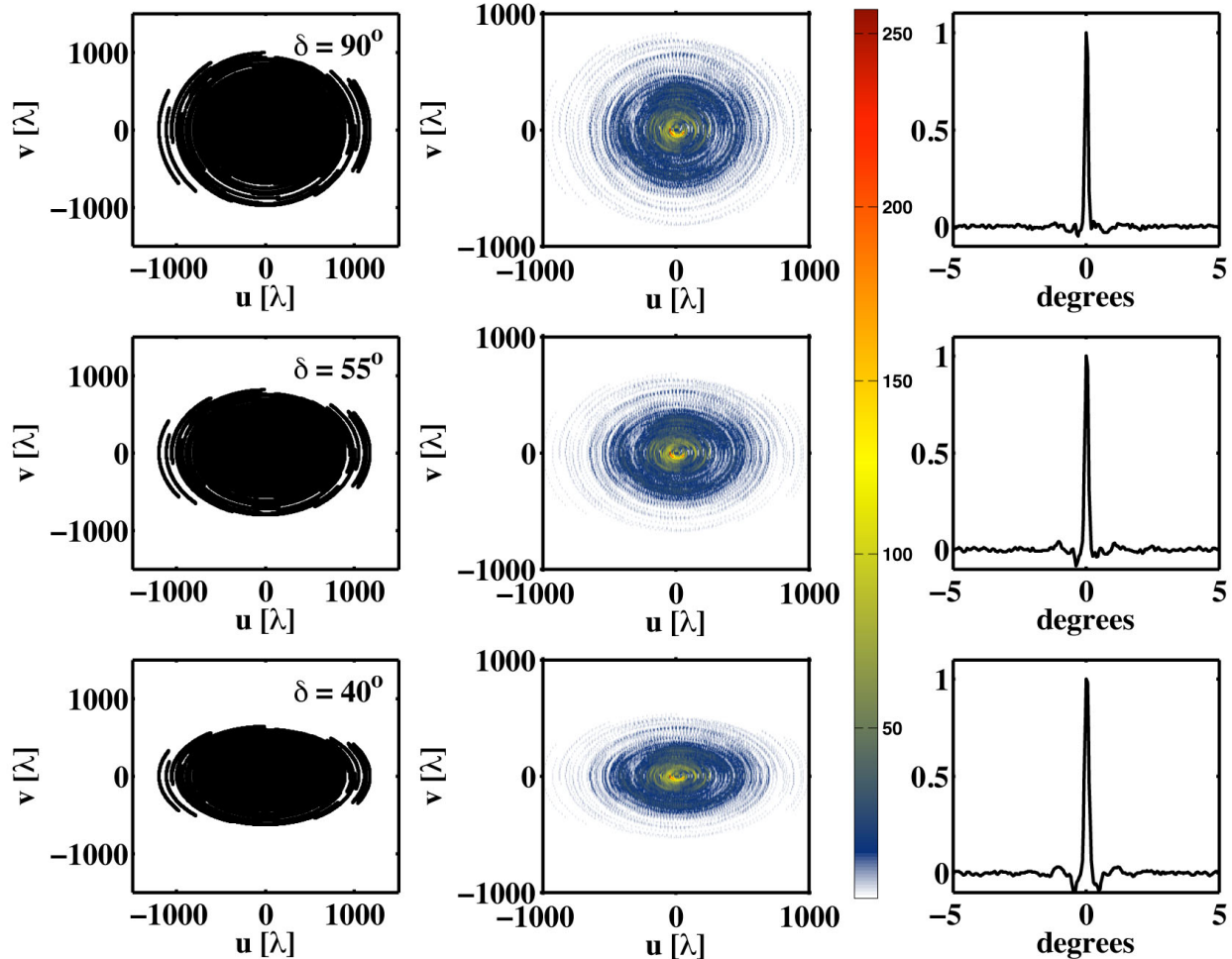


Figure 2. The first column of figures shows the uv-coverage of the LOFAR core, that will be used for the EOR experiment, for different values of the declination δ . The size of each point corresponds to the station diameter. The uv coverage is calculated for 4 hours of synthesis with 10s averaging at 150 MHz. The second column shows the corresponding uv point density. The uv plane is gridded with a cell size of 8.5 wavelengths squared. In the last column a horizontal cut of the ‘dirty’ beam is shown.

els (LSM/GSM; i.e. catalogues of the brightest, mostly compact, sources in and outside of the beam, i.e. local versus global). A further complication is the extraction of the Galactic and extragalactic foregrounds. This is a vital step in the recovery of the signal and requires good sampling of the uv-plane at all frequencies (Bowman, Morales, & Hewitt 2008, 2006; Morales, Bowman, & Hewitt 2005).

2.2 The High-Band Antennas

LOFAR will have two sets of dipoles, the Low Band Antennas (LBA) and the High Band Antennas (HBA). For the EOR experiment we are mostly interested in the HBA dipoles which cover the 110 to 220 MHz frequency range. Each dipole is a crossed dipole which enables X and Y polarization observations. Inside the station the dipoles are arranged in tiles of 4 by 4 dipoles, with 24 tiles per station inside the core (Figure 1). Radio waves are sampled with a 16-bit analog-to-digital converter to be able to cope with ex-

pected interference levels operating at either 160 or 200 MHz in the first, second or third Nyquist zone (i.e., 0–100, 100–200, or 200–300 MHz band respectively for 200 MHz sampling). The data from the receptors are filtered in 512, 195 kHz sub-bands (156 kHz sub-bands for 160 MHz sampling) of which a total of 32 MHz bandwidth (164 channels) can be used at one time. Sub-bands from all antennas are combined at the station level in a digital beamformer allowing multiple (4–6) independently steerable beams, which are sent to the central processor via a glass-fibre link that handles 0.7 Tbit/s data. The beams from all stations are further filtered into 1 kHz channels, cross-correlated and integrated. The integrated visibilities are then calibrated on 1 second intervals, to correct for the effects of the ionosphere, and subsequently images are produced. Channels with disturbing radio frequency interference (RFI) are excised (Leshem, van der Veen, & Boonstra 2000; Veen, Leshem, & Boonstra 2004b; Wijnholds, Bregman, & Boonstra 2004; Fridman & Baan 2001). For the correlation we use three racks of an IBM Blue Gene/P machine in Groningen with a total of 12288 process-

ing cores. LOFAR is a new concept in array design, a broad-band aperture array with digital beamforming. This makes LOFAR essentially qualify as a pathfinder for the Square Kilometre Array (Falcke et al. 2007).

3 MATHEMATICAL FRAMEWORK OF THE LOFAR DATA MODEL

The most important part of any physical measurement is to find a correspondence between the physical quantities and the measured quantities. In radio interferometry this is achieved through the so called measurement equations (Hamaker & Bregman 1996; Boonstra 2005). The measurement equation (ME) describes the relationship between the visibilities (correlations between the electric fields from different antennas) and the brightness distribution of the sky. We will begin by discussing briefly the different types of measurement equations and the implications for LOFAR (Smirnov & Noordam 2006; Noordam 2004, 2000). The data model presented in this paper can be easily applied to other telescopes that operate at low frequencies such as the MWA and eventually the SKA.

Astronomical radio signals appear as spatially wide-band random noise with superimposed features, such as polarization, emission and absorption lines. The physical quantity that underlies this kind of measurement is the electric field, but for convenience astronomers try to recover the intensity in the direction of the unit pointing vector \mathbf{s} , $I_f(\mathbf{s}) = \langle |E_f(\mathbf{s})|^2 \rangle$. The measured correlation of the electric fields between two sensors i and j is called the complex visibility. For Earth-rotation synthesis we assume that the telescopes have a small field of view (FOV) and that they track a position on the sky. To achieve that, a slowly time-varying phase delay has to be introduced at the receiver to compensate for the geometrical delays. The result is that the reference location appears to be at the zenith, or their chosen point in the sky (phase reference center). For a planar array, the receiver baselines can be parametrized as

$$\mathbf{r}_i - \mathbf{r}_j = \lambda[u, v, 0], \quad \lambda \equiv \frac{c}{2\pi\nu}. \quad (1)$$

where \mathbf{r}_i are the station position vectors. This system is wavelength dependent. The (scalar) measurement equation in (u, v) coordinates becomes

$$V_f(u, v) = \iint \mathcal{P}_f(l, m) I_f(l, m) e^{-i(ul+vm)} dl dm \quad (2)$$

where $\mathcal{P}_f(l, m)$ is the complex primary beam or antenna response pattern and $I_f(l, m)$ is the sky brightness distribution. This equation (van Cittert–Zernike theorem) is in the form of a 2-D Fourier transform, which is an approximation for a flat sky (Thompson, Moran, & Swenson 2001; Carozzi & Woan 2008). The visibilities are sampled for all different sensor pairs i and j , but also for different sensor locations projected on the sky, since the Earth rotates. Hence Earth-rotation synthesis traces uv tracks for each baseline (Thompson, Moran, & Swenson 2001).

3.1 The Scalar Measurement Equation

The most widely used ME is still the scalar formulation of the ME. We begin the discussion with the scalar ME and later we will also discuss the polarized version thereof. Since all processing is done with digital computers this equation must be transformed into a more convenient discretized form. The main output of the LOFAR correlator is a set of correlation matrices (Boonstra 2005; Falcke et al. 2007), $\mathbf{R}_f(t_k)$, for a set of narrow-band frequency channels

(adding up to 32 MHz bandwidth) and for a set of short-time integrations (adding up to >300 hours of integration). The connection between the correlation matrices $\mathbf{R}_f(t_k)$ and the visibilities $V_f(u, v)$ is that each entry $R_{ij}(t_k)$ of $\mathbf{R}_f(t_k)$ is a sample of the visibility function for a specific coordinate (u, v) corresponding to the baseline vector $\mathbf{r}_{ij} = \mathbf{r}_i - \mathbf{r}_j$ between telescopes i and j at time t_k (Boonstra 2005):

$$V_f(u_{ik} - u_{jk}, v_{ik} - v_{jk}) \equiv R_{ij}(t_k).$$

The noiseless scalar measurement equation (not accounting for instrumental and other distorting effects) for one short-time integration and narrow-band frequency channel, assuming the sky can be described by a set of point-sources, can then be written in terms of the correlation matrices⁷ as (Boonstra 2005; Leshem & van der Veen 2000)

$$\mathbf{R}_{k,f} = \mathbf{A}_{k,f} \mathbf{B}_f \mathbf{A}_{k,f}^\dagger \quad (3)$$

where

$$\mathbf{A}_{k,f} = [\mathbf{a}_{k,f}(\mathbf{s}_1), \dots, \mathbf{a}_{k,f}(\mathbf{s}_d)]$$

$$\mathbf{a}_{k,f}(\mathbf{s}_i) = \begin{bmatrix} e^{-i(u_{1k}l + v_{1k}m)} \\ \vdots \\ e^{-i(u_{N_{tel}k}l + v_{N_{tel}k}m)} \end{bmatrix} \quad (4)$$

$$\mathbf{B}_f = \begin{pmatrix} B_f(\mathbf{s}_1) & & \\ & \ddots & \\ & & B_f(\mathbf{s}_d) \end{pmatrix}$$

and where k is the time-ordered visibility number, \mathbf{s} is the source position vector on the celestial sphere and f the observing frequency channel number.

The vector functions $\mathbf{a}_{k,f}$ are called array response vectors in array signal processing and they are frequency dependent, but also time dependent in this case due to the rotation of the Earth (Leshem & van der Veen 2000; van Trees 2002). They describe the response of an interferometer to a source at direction $\mathbf{s} = (l, m)$ (see Figure 3).

The above formalism is trivial as long as the positions of the telescopes are well known. In reality though, the response of the array is not perfect: telescopes are not omni-directional antennas, but each one has its own properties (i.e. complex beam-shape and gain etc.). In this case the array response vectors must be redefined as

$$\mathbf{a}_{k,f}(\mathbf{s}_i) = \begin{pmatrix} \mathcal{A}_1(\mathbf{s}_i) \\ \vdots \\ \mathcal{A}_{N_{tel}}(\mathbf{s}_i) \end{pmatrix} \odot \begin{bmatrix} e^{-i(\mathbf{u}_{1k} \cdot \mathbf{s}_i)} \\ \vdots \\ e^{-i(\mathbf{u}_{N_{tel}k} \cdot \mathbf{s}_i)} \end{bmatrix}, \quad (5)$$

where \odot indicates a Hadamard (element-wise) product. The source structure can also vary with frequency. Finally, most of the received signal consists of additive noise. When the noise has zero mean and is independent among the antennas (spatially white), then

$$\mathbf{R}_{k,f} = \mathbf{A}_{k,f} \mathbf{B}_f \mathbf{A}_{k,f}^\dagger + \sigma_f^2 \mathbf{I}$$

Noise can be assumed to be Gaussian in radio-interferometers, like LOFAR. We will assume this in the remainder of this paper, and might address non-Gaussian (Thompson, Moran, & Swenson 2001) time-varying noise in future publications. Actually, system noise is

⁷ The symbol "†" stands for the Hermitian conjugation operator

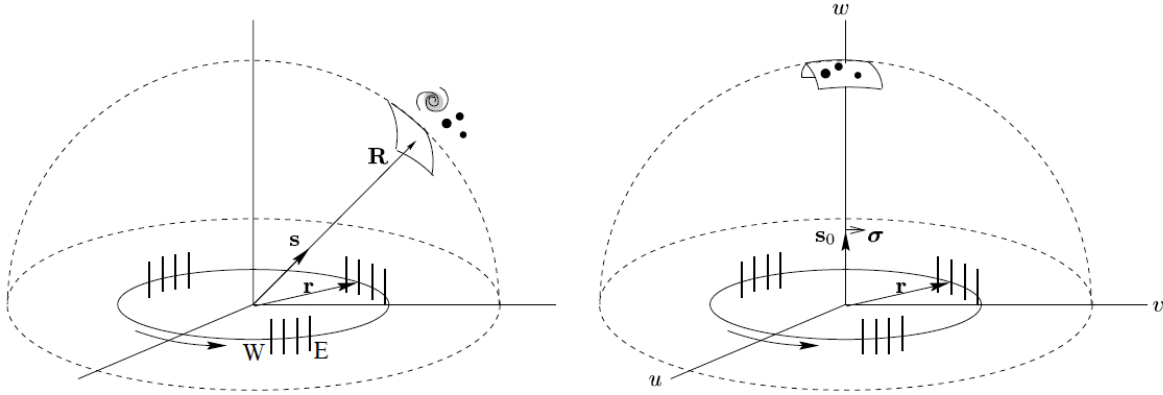


Figure 3. The sky brightness distribution before and after geometrical delay compensation, as seen by an interferometer. \mathbf{R} is the source position vector and \mathbf{s} the relevant unit vector in the direction of \mathbf{R} . \mathbf{r} is the baseline vector.

slightly different at each receiver. It is reasonable to assume that noise is spatially white: the noise covariance matrix is diagonal.

3.2 The Polarization Measurement Equation

The equations above describe the relation of the visibilities to the total intensity of the source, i.e. the classical Stokes I . To take polarization into account, several modifications are required. The use of the polarization information is of great importance for several reasons. First, this information provides insight in the physical processes that might exist in the astronomical object of interest. Second, modern telescopes like LOFAR are also inherently polarized. Third, using more information enhances the result of the data reduction process. The study of polarized light is therefore becoming an increasingly important issue in astrophysics (Tinbergen 1996).

Many matricial models have been developed to study the polarization properties of light. A proper description of the polarization properties of light relies on the concept of the coherency matrix (Born & Wolf 1999; Hamaker & Bregman 1996). This mathematical formalism holds for every band of the electromagnetic spectrum. A usual assumption is monochromatic light, but polychromatic light behaves as monochromatic for time intervals longer than the natural period and shorter than the coherence time (Gil 2007; Barakat 1963). Our mathematical model will be based on those introduced in radio-astronomy by Hamaker & Bregman (1996).

3.2.1 The Electric-Field Vector and Coherency Matrix

The effects of linear passive media on the propagated photons can be represented by linear transformations of the electric field variables. The nature of those effects, the spectral profile of the light and the chromatic and polarizing properties of the medium through which light passes, all affect the degree of mutual coherence. In general coherent interactions can be represented by the Jones calculus (Jones 1941, 1942, 1948), while incoherent interactions of polychromatic light require the Mueller calculus (Barakat 1963), since the loss of coherence needs more parameters to be described. The two components of the electric field (e.g. those received at two dipoles) can be arranged as the components a 2×1 complex vector:

$$\mathbf{e}(t) = \begin{pmatrix} E_x(t) \\ E_y(t) e^{i\delta(t)} \end{pmatrix} \quad (6)$$

where $\delta(t)$ is the relative phase. This vector includes all information about the temporal evolution of the electric field. When the parameters have no time dependence this is called the *Jones vector*. Moreover, the coherency (or polarization or density) matrix of a light beam contains all the information about its polarization state. This Hermitian 2×2 matrix is defined as

$$\mathbf{C} \equiv \langle \mathbf{e}(t) \otimes \mathbf{e}^\dagger(t) \rangle = \begin{pmatrix} \langle e_1(t) e_1^*(t) \rangle & \langle e_1(t) e_2^*(t) \rangle \\ \langle e_2(t) e_1^*(t) \rangle & \langle e_2(t) e_2^*(t) \rangle \end{pmatrix} \quad (7)$$

This is the coherency matrix of the perpendicular dipoles of a single LOFAR HBA antenna. \otimes stands for the Kronecker product and the brackets indicate averaging over time (Boonstra 2005). The coherency matrix is a correlation matrix whose elements are the second moments of the signal. Using the ergodic hypothesis the brackets can be considered as ensemble averaging. Due to its statistical nature its eigenvalues ought to be non-negative. The normalized version of this matrix $\hat{\mathbf{C}} = \frac{\mathbf{C}}{\text{tr}(\mathbf{C})}$ contains information about the population and coherencies of the polarization states (Fano 1957). This object is the equivalent of the single brightness point in the scalar version of the theory.

3.2.2 The Stokes Parameters

Above we discussed the statistical interpretation of the coherency matrix. Now we can also introduce a geometrical description: the measurable quantities Stokes I , Q , U and V arise as the coefficients of the projection of the coherency matrix onto a set of Hermitian trace-orthogonal matrices, the generators of the unitary $SU(2)$ group plus the identity matrix (see Appendix A1). Parameters with direct physical meaning can be derived from the corresponding measurable quantities. The Stokes parameters are usually arranged as a 4×1 vector,

$$\mathbf{s} = \begin{pmatrix} I \\ Q \\ U \\ V \end{pmatrix}.$$

An alternative notation, that will be derived in Appendix A is the 2×2 Stokes matrix:

$$\mathbf{S} = \frac{1}{2} \begin{pmatrix} I+Q & U-iV \\ U+iV & I-Q \end{pmatrix} \equiv \mathbf{C}, \quad (8)$$

which relates the measured coherency matrix quantities to the Stokes parameters (Born & Wolf 1999).

3.2.3 The Jones Formalism

An adequate method to describe a non-depolarizing system is the Jones formalism. It represents the effects on the polarization properties of an EM wave after the interaction with such a system. For passive, pure systems, the electric field components of the light interacting with them is given by the corresponding Jones matrix \mathbf{J} ,

$$\mathbf{e}' = \mathbf{J}\mathbf{e}.$$

As both the initial and final fields can fluctuate, it is useful to describe the properties of partially polarized light with the coherency matrix. Thus,

$$\begin{aligned} \mathbf{C}' &= \langle \mathbf{e}' \otimes \mathbf{e}'^\dagger \rangle = \langle (\mathbf{J}\mathbf{e}) \otimes (\mathbf{J}\mathbf{e})^\dagger \rangle \\ &= \langle \mathbf{J}\mathbf{e} \otimes \mathbf{e}^\dagger \mathbf{J}^\dagger \rangle = \mathbf{J} \langle \mathbf{e} \otimes \mathbf{e}^\dagger \rangle \mathbf{J}^\dagger = \mathbf{J}\mathbf{C}\mathbf{J}^\dagger \end{aligned} \quad (9)$$

As we are dealing with interferometry, the two \mathbf{J} matrices can come from two different telescopes. The effects on the electric field vectors in the coherency matrix \mathbf{C}' can be written as an operation of these Jones matrices on the original unaffected coherency matrix \mathbf{C} . As we already mentioned, the coherency matrix can also be written as a four vector with $\mathbf{c} = (\langle e_1 e_1^* \rangle, \langle e_1 e_2^* \rangle, \langle e_2 e_1^* \rangle, \langle e_2 e_2^* \rangle)$. This vector is related to the Stokes vector via (Parke 1948)

$$\mathbf{s} = \mathbf{L}\mathbf{c} \quad \text{with} \quad \mathbf{L} = \begin{pmatrix} 1 & 0 & 0 & 1 \\ 1 & 0 & 0 & -1 \\ 0 & 1 & 1 & 0 \\ 0 & -i & i & 0 \end{pmatrix}. \quad (10)$$

The matrix has the following property $\mathbf{L}^{-1} = \frac{1}{2}\mathbf{L}^\dagger$. Using the properties of the Kronecker product we then find, in terms of Stokes parameters, that

$$\begin{aligned} \mathbf{s}' &= \mathbf{L} \langle \mathbf{J}\mathbf{e} \otimes (\mathbf{J}\mathbf{e})^\dagger \rangle = \mathbf{N}\mathbf{s} \\ \mathbf{N} &= \mathbf{L} (\mathbf{J} \otimes \mathbf{J}) \mathbf{L}^{-1} \\ &\quad \text{with} \\ \mathbf{N}_{kl} &= \frac{1}{2} \text{tr} (\sigma_k \mathbf{J} \sigma_l \mathbf{J}^\dagger). \end{aligned} \quad (11)$$

where σ_i are the Pauli matrices (Appendix A1). A Jones matrix can represent a physically realizable state as long as the transmittance condition (gain or intensity transmittance) holds; that is, the ratio of the initial and final intensities must be $0 \leq g \leq 1$. The reciprocity condition describes the effect when the output signal follows the path in the inverse order. For every proper Jones matrix $\mathbf{e}' = \mathbf{J}^\dagger \mathbf{e}$. This result does not hold when magneto-optic effects are present. In this case the Mueller–Jones matrices have to be used. If a Jones matrix represents a physically realizable state the reciprocal matrix also represents a physical effect.

4 THE LOFAR MEASUREMENT EQUATION

LOFAR stations consist of tiles of 4×4 crossed dipoles which allow for full Stokes measurements. If we have N_{tel} stations each with two polarization degrees of freedom, then the $2N_{\text{tel}}$ electric fields

can be stacked into a single vector and the correlation matrix can be generalized to the following form

$$\begin{aligned} \mathbf{V} &= \begin{pmatrix} \langle E_x(\mathbf{r}_i) E_x^*(\mathbf{r}_j) \rangle & \langle E_x(\mathbf{r}_i) E_y^*(\mathbf{r}_j) \rangle \\ \langle E_y(\mathbf{r}_i) E_x^*(\mathbf{r}_j) \rangle & \langle E_y(\mathbf{r}_i) E_y^*(\mathbf{r}_j) \rangle \end{pmatrix} \\ &= \begin{pmatrix} V_{xx} & V_{xy} \\ V_{xy} & V_{yy} \end{pmatrix} \end{aligned} \quad (12)$$

for a linear polarization basis. Note that each element of \mathbf{V} , V_{ij} is not Hermitian for $i \neq j$, but $V_{ij} = V_{ji}^\dagger$, so that \mathbf{V} remains Hermitian (Hamaker & Bregman 1996). Here we have denoted explicitly the correlation from the X and Y oriented dipoles.

Let \mathbf{A}_{il} be the position dependent polarization multiplication matrix. This is the array response matrix (as it is termed in the language of communication theory) or in the Hamaker formalism the Jones matrix. The array response vector must take into account the different physical and instrumental effects that affect the signal through its path from the source to the recorder, like ionospheric Faraday rotation, parallactic offsets, the geometric delay and instrumental gains (and leakages). These effects are represented by the Jones matrices. So we can write the measurement equation in the form (Boonstra 2005; Veen, Leshem, & Boonstra 2004a)

$$\mathbf{V}_{ijl} = \mathbf{A}_{il} \mathbf{B}_l \mathbf{A}_{jl}^\dagger + \mathbf{N}_{\text{noise}}$$

where the different effects \mathbf{A} in the array response vector must be introduced in the exact order in which they affect the signal. The index l is the pixel number and the index i, j represent antennas i and j respectively. The algebra of complex Jones matrices is obviously non-commutative, i.e. the ordering of the matrices matters. The physical meaning of this is that the results of the different effects on the incoming electromagnetic wave are not linear.

4.1 Individual Jones matrices

In this section we give a brief overview of the instrumental parameters (Jones matrices) which are used for our data simulations, their importance, and which parameters we use and perturb.

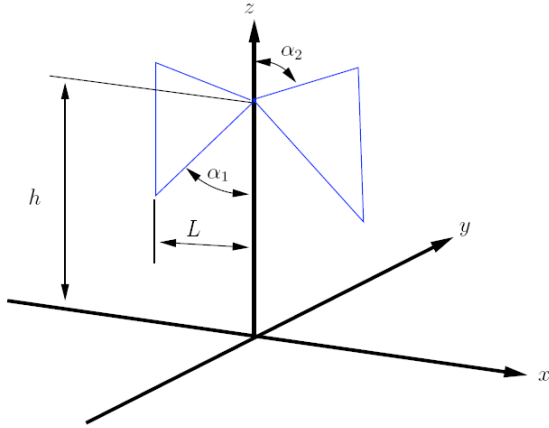
F: Ionospheric Faraday Rotation The ionosphere is birefringent, such that one handedness of circular polarization is delayed with respect to the other, introducing a dispersive phase shift in radians

$$\Delta\phi \approx 2.62 \times 10^{-13} \lambda^2 \int B_{\parallel} n_e ds (\text{SI})$$

It rotates the linear polarization position angle and is more important at longer wavelengths, at times close to the solar maximum and at Sunrise or Sunset, when the ionosphere is most active and variable (Eliasson & Thidé 2008; Norin et al. 2008; Eliasson & Thidé 2007; Thidé 2007; Spoelstra 1996, 1995; van Velthoven & Spoelstra 1992; Spoelstra & Yang 1990; Spoelstra & Schilizzi 1981). The Faraday rotation Jones matrix is a real-valued rotation matrix:

$$\mathbf{F} = \begin{pmatrix} \cos \Delta\phi & -\sin \Delta\phi \\ \sin \Delta\phi & \cos \Delta\phi \end{pmatrix}$$

To model the Total Electron Content (TEC) (van der Tol & van der Veen 2007), we use a Gaussian random field with Kolmogorov-like turbulence. We use a cut-off at scales that correspond to the maximum and minimum baselines of WSRT (Westerbork Synthesis Radio Telescope), similar to those of LOFAR. Initial model parameters have been obtained from WSRT data, taken at similar frequencies, baselines and time intervals to our planned LOFAR observations. Moreover, the WSRT is located approximately 50 km from the LOFAR core in Exloo and as such the WSRT provides a

Figure 4. The design of a LOFAR HBA dipole antenna element.

good test-bed for forthcoming LOFAR observations and expected ionospheric effects.

P: Parallaxic Angle This matrix describes the orientation of the sky in the telescope’s field of view, or similarly the projection of the dipoles onto the sky. It has the mathematical structure of a rotation matrix and rotates the position angle of linearly polarized radiation incident on the dipoles. It should in principle be analytically and deterministically known, and its variation provides leverage for determining polarization-dependent effects. It can also be used at the initial stages to determine dipole orientation errors.

$$\mathbf{P} = \begin{pmatrix} \cos \chi & -\sin \chi \\ \sin \chi & \cos \chi \end{pmatrix}$$

where χ is the parallaxic angle. We shall include this matrix in the antenna voltage pattern matrix.

E: Antenna Voltage Patterns The LOFAR telescope HBA stations consists of crossed bowtie dipole pairs. Like every antenna, they have a directionally dependent gain which is important when the angular size of the region on the sky is comparable to $\sim \lambda/D$, where D is the station diameter. At low frequencies when the radio sky is dominated by point sources, wide-field techniques are required as well. To determine the antenna voltage pattern to first order, we assume an analytic model of the dipole pairs: the basic parameters as shown in Fig. 4 have the following values: $L=0.366$ m, $h=0.45$ m, $\alpha_1=50$ deg and $\alpha_2=80$ deg.

As the Earth rotates, the dipoles rotate with respect to the sky. This causes the polarization coordinate system to rotate (unlike e.g. the WSRT which has an equatorial mount) and we must thus correct for this effect. For a pair of crossed dipoles along the X and Y axes the relevant Jones matrix \mathbf{E} can be written as:

$$\mathbf{E} = \begin{pmatrix} E_\theta \left(\frac{\pi}{2} - \theta, \phi - \frac{\pi}{4} \right) & E_\phi \left(\frac{\pi}{2} - \theta, \phi - \frac{\pi}{4} \right) \\ E_\theta \left(\frac{\pi}{2} - \theta, \phi - \frac{3\pi}{4} \right) & E_\phi \left(\frac{\pi}{2} - \theta, \phi - \frac{3\pi}{4} \right) \end{pmatrix}$$

where ϕ and θ are the polar and azimuthal angles of the beam pattern. We assume that the X and Y dipoles have the same beam pattern. Because of the spatial distribution of the dipoles within a station, each dipole has a different delay for the reception of an electromagnetic wave coming from a source. If we assume a narrowband system, one can correct for this by shifting the phase for the signal of each dipole element of the stations (i.e. introducing an effective delay). We have an analytical model for the HBA antenna

element beam and we assume that the dipoles are uniformly distributed to form a circular array. Thus, we ignore the tile structure, for the purposes of the current paper. If we need to form a station-beam in an arbitrary direction inside the dipole/ tile beam, we can do it by properly weighting the signals of each element and adding delays. Another simpler way to proceed, which is sufficient for the purposes of this paper, is to calculate the beam shape of an axially symmetric, uniformly distributed array of elements and then multiply it with the primary element pattern that we calculated above. We also assume that the thin-wire approximation holds.

D: Polarization Leakage and Instrumental Polarization Radio-interferometers usually measure the full set of Stokes parameters simultaneously. Measuring the polarization properties of Galactic diffuse emission as well as the extragalactic sources is an important aspect of the EoR-KSP. The polarization fraction of most astronomical sources is typically low, of the order of few per cent. Measuring it with accuracy is thus challenging, but important in order to extract scientific information from it. Cross-polarization or polarization leakage is an instrumental contamination that couples orthogonal Jones vectors. The dipoles are not ideal, so orthogonal polarizations are not perfectly separated. A slight tilt between the dipoles, for example, can change the polarization reception pattern. This must be taken into account, especially when we aim to reach a high dynamic range in the images. It is supposed to be of the order of less than a few per cent and because it is a geometrical factor, we expect that it is frequency dependent. The relevant Jones matrix can be written in the form of a unitary matrix (Heiles et al. 2001; Heiles 2002; Bhatnagar & Nityananda 2001; Reid et al. 2008):

$$\mathbf{D} = \begin{pmatrix} \sqrt{1-d} & -\sqrt{d}e^{i\psi} \\ \sqrt{d}e^{-i\psi} & \sqrt{1-d} \end{pmatrix} \quad (13)$$

where d is a generally small constant of the order of 10^{-6} . This is a first-order approximation to behaviour that might prove more complex. However, it is very important to know this parameter as it can convert unpolarized radiation, such as the EoR signal, into polarized radiation. This matrix has almost the structure of a rotation matrix. The difference is the inclusion of the phase ψ . When ψ equals zero, polarization leakage converts Q to U or E to B -modes [rotation across the equator of the Poincaré sphere (Heiles et al. 2001)]. When the phase term is significant, polarization leakage leads to mixing Q , U and V . Polarization leakage manifests itself as closure errors in parallel hand visibilities and the leakage-induced closure phase and the Pancharatnam phase of optics (Berry 1987). This phase arises when the state of polarization of the light is transformed following a closed path in the space of states of polarization, which is known as the Poincaré sphere (Born & Wolf 1999). Another type of distortion is the instrumental polarization. The dipole and station designs as well as the processing done can contribute to such effects. LOFAR uses linearly polarized dipoles. The interferometric measurement of the Stokes parameters U and V using two different dipoles is made by forming the “cross-handed” products of the signals. If for any reason the signals are received with different gains, this would lead to a certain fraction of polarization. This can be modelled as:

$$\mathbf{D}_p = \begin{pmatrix} d_1 & 0 \\ 0 & d_2 e^{i\psi} \end{pmatrix}, \quad (14)$$

where d_1 , d_2 are the different X and Y gains. We assume that the instrumental polarization axis lies along the axis defined by the matrix basis to write this equation. In such case Q does not leak into

U , but still I leaks onto Q . With a carefully chosen basis (see Appendix A) I does not leak into U .

G: Complex baseline-based electronic gain This matrix accounts for all amplitude-phase- and frequency-independent effects of the station electronics. It shows a slow variation of the order of 1–2% over a day. It has the form:

$$\mathbf{G} = \begin{pmatrix} g_X & 0 \\ 0 & g_Y \end{pmatrix},$$

where g_X and g_Y are complex numbers. It is one of the most common calibration parameters and the one commonly solved for in the classical self-calibration loop.

B: Bandpass Compensating for change of gain with frequency is called bandpass calibration. This matrix is similar to \mathbf{G} and describes the frequency-dependence of the antenna electronics. Station digital poly-filters, used to select the frequency passband, are not perfectly square, but they are deterministically known and their bandpass behavior is expected to be quite stable over large periods of time. Its generic form is:

$$\mathbf{B} = \begin{pmatrix} b_x(f) & 0 \\ 0 & b_y(f) \end{pmatrix}$$

The b are real numbers. We model both \mathbf{B} and \mathbf{G} parameters as slowly time-varying functions with additive white noise as the initial commissioning tests for LOFAR suggest.

K: Fourier kernel This term has traditionally been called the Fourier kernel. For larger fields of view and/or longer baselines the 2-D Fourier transform relationship between the sky and the measured visibilities is no longer a good approximation. This term describes a phase shift that accounts for the geometrical delay for the signals received by telescopes i and j . Let x , y and z be the antenna positions in a coordinate system that points to the West, South and the Zenith respectively. We can provide the directions on the sky in terms of the directional cosines l, m, n . We assume that the sky is a unit sphere so that $l^2 + m^2 + n^2 = 1$ (Thompson, Moran, & Swenson 2001). Since the X and Y dipoles are co-located, the relevant Jones matrix takes the following simple form:

$$\mathbf{K} = e^{-i[ul+vm+w(\sqrt{1-l^2-m^2}-1)]} \begin{pmatrix} 1 & 0 \\ 0 & 1 \end{pmatrix}$$

This matrix should also be well determined, but solving for it can help to estimate the antenna positions, the electronic path lengths, the clock errors etc. For this the concept of the array manifold is useful (Manikas 2004) It also provides astrometric information by solving for l, m and n , which are the direction cosines of the sources on the sky.

4.2 The Final Form of the Measurement Equation

All the above effects can be combined in order to form the Hamaker–Bregman–Sault measurement equation. The equation looks like:

$$V_{ij}^{\text{obs}} = \int_{l,m,n} dl dm \left(\mathbf{A}_i \otimes \mathbf{A}_j^\dagger \right) \mathbf{c}(l, m), \quad \text{with} \quad (15)$$

$$\mathbf{A}_i = \mathbf{K}_i \mathbf{B}_i \mathbf{G}_i \mathbf{D}_i \mathbf{E}_i \mathbf{P}_i \mathbf{T}_i \mathbf{F}_i$$

$$\mathbf{A}_j^\dagger = \mathbf{F}_j^\dagger \mathbf{T}_j^\dagger \mathbf{P}_j^\dagger \mathbf{E}_j^\dagger \mathbf{D}_j^\dagger \mathbf{G}_j^\dagger \mathbf{B}_j^\dagger \mathbf{K}_j^\dagger$$

where $\mathbf{c} = \text{vec}(\mathbf{C})$ is the 4×1 source coherency vector in the l, n, m system⁸.

If we assume that the sky can be described as a closely-packed collection of point-sources, then the measurement equation can be rewritten as:

$$V_{ij}^{\text{obs}} = \sum_{l,m} \mathbf{A}_i(l, m) \mathbf{C}(l, m) \mathbf{A}_j^\dagger(l, m)$$

where \mathbf{C} is the coherency matrix of a single point-source at (l, m) . For a single point-source with the rest of the sky blank this simplifies further to

$$V_{ij}^{\text{obs}} = \mathbf{A}_i(l, m) \mathbf{C}(l, m) \mathbf{A}_j^\dagger(l, m).$$

We must note that this equation is linear over the coherency matrix \mathbf{C} , but not over the Jones matrices \mathbf{A} . We reiterate that the individual Jones matrices that form the matrix products \mathbf{A} , are not in general commutative. Their order follows the signal path. The form of this equation is quite complicated. Every element in the new matrix is a non-linear function of all the parameters that appear in the various Jones matrices.

It has been proposed (Hamaker 2006, 2000a) that we can self-calibrate the generic \mathbf{A} matrix, apply post-calibration constraints to ensure consistency of the astronomical absolute calibrations, and recover full polarization measurements of the sky. This is an interesting idea for low-frequency arrays, where isolated calibrators are unavailable (due to the fact that such arrays see the whole sky). This just emphasizes the fact that calibration and source structure are tied together - one cannot have one without the other.

4.3 Additive errors

The ultimate sensitivity of a receiving system is determined principally by the system noise. The discussion of the noise properties of a complex receiving system like LOFAR can be lengthy (Lopez & Fabregas 2002; de Bruyn et. al 2007), so we concentrate for our purposes on some basic principles. The theoretical *rms* (root mean square) noise level in terms of flux density on the final image is given by (Thompson, Moran, & Swenson 2001)

$$\sigma_{\text{noise}} = \frac{1}{\eta_s} \times \frac{\text{SEFD}}{\sqrt{N \times (N-1) \times \Delta\nu \times t_{\text{int}}}} \quad (16)$$

where η_s is the system efficiency that accounts for electronic, digital losses, N is the number of substations, $\Delta\nu$ is the frequency bandwidth, t_{int} is the total integration time and SEFD is the System Equivalent Flux Density. The system noise we assume to have two contributions: the first comes from the sky and is frequency dependent ($\approx \nu^{-2.55}$) (Shaver et al. 1999; Jelic et al. 2008) and the second comes from from the receivers. The scaling of the A_{eff} , the effective collecting area of the antennae with frequency, introduces also a frequency dependence. We also assume that the distribution of noise over the uv -plane at one frequency is Gaussian, in both the real and imaginary part of the visibilities. For a 24-tile LOFAR core station, the SEFD will be around 2000 Jy ($\eta \sim 0.5$), depending on the final design (de Bruyn et. al 2007). This means that we

⁸ Here we use the Kronecker product identity $\mathbf{A}\mathbf{X}\mathbf{B} = \mathbf{C} \Leftrightarrow (\mathbf{B}^T \otimes \mathbf{A}) \text{vec}(\mathbf{X}) = \text{vec}(\mathbf{C})$. We can then solve for \mathbf{X} , when $(\mathbf{B}^T \otimes \mathbf{A})$ is invertible (Golub & Loan 1989). This way the measurement equation can be transformed into a linear equation.

can reach a sensitivity of 520 mK at 150 MHz with 1 MHz bandwidth in one night of 4 hours of observation. Accumulating data from a hundred nights of observations brings this number down to ~ 52 mK. We will assume a constant noise estimate of this magnitude for each pixel in the remainder of the paper. The noise is uncorrelated between different telescopes and different signals, so that we can write the noise matrix in the form:

$$\mathbf{N} = \begin{pmatrix} \langle \mathbf{n}_i \mathbf{n}_j^* \rangle_1 & & 0 \\ & \ddots & \\ 0 & & \langle \mathbf{n}_i \mathbf{n}_j^* \rangle_{N_{\text{tel}}} \end{pmatrix} \quad (17)$$

where $\mathbf{n}_i = \{n_i^{xx}, n_i^{yy}\}$.

We are now in a situation that we can start to simulate realistic data-sets for LOFAR.

5 REALISTIC LOFAR-EOR-KSP DATA SIMULATIONS

In this section, we will describe the LOFAR instrumental response simulations and the inversion method used to enhance the result of the primary calibration. The simulation consists of two steps: (i) the forward step, where we use a realistic model of the LOFAR response function, including all instrumental effects and noise to generate simulated LOFAR EoR data, and (ii) an inversion step where we use the data model with realistic solutions and error range for the data model parameters, to obtain the underlying visibilities. In this subsection we shall consider the forward step. The data model is based on the Hamaker–Bregman–Sault measurement equation, as described in the previous sections, and we use an “onion-layer” approach to predict the instrumental response, as is suggested by the order of the Jones matrices in the Measurement Equation. First, we must obtain a representation of the Fourier Transform of the sky, as it is perceived by an interferometer. To achieve this we predict the values of the \mathbf{K} Jones matrix. This includes calculating the u , v and w terms as well as the l , m and n direction cosines. For the purpose of this paper we calculated them for six hours of integration and ten seconds of averaging. The centre of the sky maps is at $\delta_c = 52^\circ$ and $\alpha_c = 12$ hours.

The next step is to predict the ‘true’ uncorrupted visibilities for different sky realizations. Those are the visibilities as seen by a perfectly calibrated and noiseless instrument. In this step, the source structure and the calibration problem are linked together in the visibilities (Pearson & Readhead 1984; Hamaker 2006, 2000a,b, 1999), thus we need to investigate the performance of the inversion method, using sky models with different complexities (see subsection 5.3). In this paper we apply the method to the galactic diffuse emission superimposed on the cosmological signal. In the future we will also consider a collection of point sources (this will be useful for the construction and improvement the Local Sky Model).

The simulated maps between 200 and 110 MHz were created at a high frequency resolution (100 kHz) corresponding to the LOFAR EoR data-set resolution and were subsequently binned in frequency using a 1 MHz moving average box function. Each simulated visibility data-set has a size of approximately 100 MB. We produced data-sets for 128 frequency channels (reduced from 320 that will be used during the real experiment).

The simulation, inversion and signal extraction algorithms are implemented in MATLAB, with extensive use of MATLAB executables files, to speed up the most often visited loops. Due to the parallel nature of the procedures, the Distributing Computing Toolbox is used, while many BLAS operations and the FFT are implemented using the relevant NVIDIA CUDA 2.0 libraries, and run on

a single Tesla S870 system. For the rest we used a 16-way SMP workstation with 32 GB of RAM and sufficient disk space.

5.1 Cosmological signal and foregrounds simulations

We start by discussing the cosmological signal maps that we used in the simulation. The cosmological 21-cm signal is generated in a simplified manner, but sufficient for our purposes. We generate a contiguous cube of dark matter density from redshift $z \sim 6$ to $z \sim 12$ (corresponding to frequencies of around 110 MHz to 200 MHz) as described in Thomas et al. (2008), from equally spaced outputs in time of an N-body simulation. We employ a comoving $100 h^{-1}$ Mpc, 256^3 particles dark matter only simulation, using GADGET 2. We furthermore assume a flat Λ CDM universe and set the cosmological parameters to $\Omega_m = 0.238$, $\Omega_b = 0.0418$, $\Omega_\Lambda = 0.762$, $\sigma_8 = 0.74$, $n_s = 0.951$ and $h = 0.73$, in agreement with the WMAP3 observations (Spergel et al. 2007).

The ratio between the baryons (basically atomic hydrogen and helium) to dark matter was set to $\Omega_b/\Omega_{\text{DM}} \approx 0.2$. Atomic hydrogen is assumed to follow an analytical ionization history of exponential nature as $1 + \exp(z - z_{\text{ion}})^{-1}$, where z_{ion} differs for each line-of-sight as $10 \pm N(0, 1)$, where $N(0, 1)$ is a normal distribution with mean zero and dispersion one. This is done to mimic a possible spread in redshift during which the reionization occurs. We plan to use a more realistic cosmological signal in the future, but for our current purposes (i.e. testing the inversion process), this is sufficiently complex.

For each of the foreground components, a $5^\circ \times 5^\circ$ map is generated in the same frequency range (between 110 and 200 MHz) pertaining to the LOFAR–EoR experiment. *In this paper, we use only simulations of the Galactic diffuse synchrotron emission and of radio galaxies. More complex foreground realizations are under investigation and we will be considering them in future work.*

Of all components of the foregrounds, galactic diffuse synchrotron emission (GDSE) is by far the most dominant and originates from the interaction between free electrons in the interstellar medium and the Galactic magnetic field. The intensity of the synchrotron emission can be expressed in terms of the brightness temperature T_b and its spectrum is close to a featureless power law $T_b \sim \nu^\beta$, where β is the brightness temperature spectral index.

At high Galactic latitudes the minimum brightness temperature of the GDSE is about 20 K at 325 MHz with variations of the order of 2 per cent on scales from 5–30 arcmin across the sky (de Bruyn et al. 1998). At the same Galactic latitudes, the temperature spectral index β of the GDSE is about -2.55 at 100 MHz (Shaver et al. 1999; Rogers & Bowman 2008) and steepens towards higher frequencies, but also gradually changes with position on the sky (e.g. Reich & Reich 1988; Platania et al. 1998).

In the four dimensional (three spatial and one frequency) simulations of the GDSE, all its observed characteristics are included: spatial and frequency variations of brightness temperature and spectral index, as well as brightness temperature variations along the line of sight. The spatial distribution of the 3D amplitude and brightness temperature spectral index of the GDSE are generated as Gaussian random fields, while along the frequency direction we assume a power law. The final map of the GDSE at each frequency is obtained by integrating the 4D cube along one spatial direction. All spatial and frequency properties of the simulated GDSE are normalized to match the values of observations. In addition to the simulations of the total brightness temperature, polarized Galactic synchrotron emission maps are also produced, that include multiple Faraday screens along the line of sight. For a

detailed explanation of the GDSE emission simulations in total and polarized brightness temperature see Jelic et al. (2008).

5.2 The uncorrupted visibilities

The prediction of the visibilities for simple intensity distribution like point-sources and Gaussian distributions is straightforward. This is not the case for diffuse emission with complex structure. There are two approaches in this case. In the discrete version of the problem, one can either use a very high resolution map and then assume that each pixel is a point source, taking into account the linearity of the ME over the brightness distribution, or one can find a proper representation of the sky distribution (i.e. shapelets) and use a carefully chosen gridding-convolution function on the uv-plane. Image plane effects need to be computed locally, as they affect relatively small scales and thus, they have a small convolution footprint. This is the approach of the MeqTree/UVBrick software (Smirnov & Noordam 2006) which is used for predicting uv-data of extended sources or of multiple point sources. Despite the computational gains of this method, we shall use the more direct and precise multiple point-source prediction. This is done in order to preclude the introduction of spurious distortions on the simulated cosmological signal as well as to retain the high-resolution of the image-plane effect predictions. The sky brightness distribution can be split into patches in order to increase the speed of execution at the expense of additional phase-shifts (i.e. a shift in (l, m, n) , the phase center of the image, corresponds to a phase shift of the Fourier kernel). In that case each discrete Fourier Transform and each frequency channel is independent, which yields an embarrassingly parallel computational process.

In our matrix formulation the operation performed becomes

$$\mathbf{V}_{\text{true},f}(u, v, w) = \sum_i^{N_{\text{pix}}} \mathbf{K}_{i,f} \mathbf{B}_{i,f} \mathbf{K}_{i,f}^\dagger,$$

where $\mathbf{B}_{i,f}$ is coherency the matrix of pixel i on a grid at each frequency f , and $\mathbf{K}_{i,f}$ is the corresponding Fourier kernel in the direction of pixel i . The same approach holds for the point-sources as well, which can have any given position. Hence, we can incorporate the different components of our sky model into a single formalism. Another reason for our preference for this method, is that the inversion of the above equation is equivalent to a deconvolution process. We shall discuss this in more detail in the following subsection.

5.3 Simulations of the instrumental response

In this section, we describe the different effects the instrument and ionosphere have on the observed visibilities. These can be split in three categories: image-plane effects, uv-plane effects and noise.

5.3.1 Image-plane effects

As we saw, the array response matrix \mathbf{A} is composed of multiple effects, namely:

- Faraday rotation
- Ionospheric phase fluctuations
- Antenna voltage pattern
- Polarization leakage and instrumental polarization
- Parallaxic angle rotation
- Fourier kernel

The effects that depend on $s = (l, m, n)$ are commonly called image-plane effects. We apply them directly on the images before taking into account the \mathbf{K} Jones matrix. This is because they are direction-dependent gains or rotations of the coherency matrix. They transform each pixel on the maps in a different way. In the uv-plane, they enter as convolutions of the visibilities. For now, we ignore the parallaxic angle \mathbf{P} Jones matrix, because its terms should be known to very high precision a priori, and depend only on the rotation of the sky inside the station primary beam pattern.

We only consider the beam pattern and the ionospheric Faraday rotation and phase delays. We use the LOFAR HBA dipole beam patterns, as well as the HBA station patterns provided in an ASTRON⁹ technical report, by Yatawatta (2007). They depend on the element geometry and the station layout. Initial engineering results from Brentjens, Yatawatta and Wijnholds (unpublished) indicate that they are stable over a time interval of ~ 8 hours. We normalize the response at the phase center to one. Slight misalignment of the dipoles, being not precisely orthogonal, would lead to a different polarized beam pattern response. Because we are not correlating each dipole pair independently, but we are actually doing aperture synthesis between entire stations, we do not have the information needed to correct this effect on a per dipole basis. In the simulations we assume that this effect is included in the errors of the relevant Jones matrices. We therefore include the net effect in the errors of the complex beam pattern.

The other two image-plane effects that we shall consider in this paper are the ionospheric phase and the Faraday rotation. We assume that the ionosphere consists of a single layer at an altitude of 250 km above the ground. We assume a velocity with a mean of 200 km h⁻¹ and a variance of 10 km h⁻¹. This is done in order to simulate the turbulent temporary motion of the traveling ionospheric disturbances (TID). We use five directions with different velocities. In such case the vertical and the slant Total Electron Contents (TEC) are equal. We assume that the TEC distribution is a random fields consistent with Kolmogorov-type turbulence. It has a mean value of 20 TECUs (1 TECU = 10¹⁶ electrons per m²) and a variance of ~ 1 TECU as in Fig 5. Each station sees approximately 20×20 square kilometers of the ionosphere, depending on the frequency. We simulated a larger patch, though, of 50×50 square kilometers. The ionospheric phase-delay introduced would be

$$\Delta\tau_{\text{ion}} = -\frac{40.3\text{m}^3\text{s}^{-2} \cdot \text{TEC}_{\text{src}}}{\nu^2}, \quad (18)$$

where TEC_{src} is the TEC along the line of sight, c is the speed of light and ν is the observing frequency (Spoelstra & Yang 1990). The form of the ionospheric delay Jones matrix is then

$$\mathbf{Z} = \mathbf{I}e^{i\Delta\tau_{\text{ion}}}$$

and the Ionospheric Faraday rotation is

$$\mathbf{F} = \begin{pmatrix} \cos\left(\frac{\text{RM}}{\nu^2}\right) & -\sin\left(\frac{\text{RM}}{\nu^2}\right) \\ \sin\left(\frac{\text{RM}}{\nu^2}\right) & \cos\left(\frac{\text{RM}}{\nu^2}\right) \end{pmatrix} \quad (19)$$

where RM is the rotation measure (Brentjens & de Bruyn 2005). The rotation measure in SI units is defined as

$$\text{RM} = \frac{e^3}{8\pi^2\epsilon_0 m^2 c^4} \int_0^d n_e B_{\parallel} ds \quad (20)$$

⁹ <http://www.astron.nl>

where ϵ_0 is the vacuum permittivity, with $B_{||}$ the magnetic field, m the mass of the electron, e the charge of the electron and n_e the electron density. From the simulated maps we construct the coherency matrix for every pixel of the maps. We then apply the image-plane effects on the maps and apply the \mathbf{K} Jones matrix to bring them to the uv-plane.

5.3.2 uv-plane effects

The next category of instrumental effects is the uv-plane effects:

- Complex gains.
- Frequency bandpasses.

The LOFAR gains and especially the bandpasses are expected to be stable over the period of one night with temporal variations of the order of two per cent. The bandpass response is well known and also well behaved. For this reason, the bandpass and complex gain effects together are handled in a single Jones matrix \mathbf{G} . Actually, the bandpasses are the frequency dependent parts of the instrumental complex gains. The frequency dependent gain can be approximated as:

$$\mathbf{G}(f, t) = \begin{pmatrix} G_1 & 0 \\ 0 & G_2 \end{pmatrix} \quad (21)$$

$$G_{\{1,2\}} = g_{\{1,2\}} \left(1 + 10^{-2} \sin(\omega_{\text{cts}} t)\right) [1 + \gamma(\nu - \nu_0)],$$

where $g_{\{1,2\}}$ are the complex gain coefficients, ω_{cts} is the cyclic frequency that corresponds to the correlation time scale of the gain solutions, γ is constant with a small value and $\nu_0 = 150$ MHz.

Since there are no HBA station cross-correlations available at the moment, we used the WSRT radio telescope solutions, scaled up as a function of collecting area. For that we used the gain solutions from a deep survey of a few fields carried out by the LOFAR-EoR KSP team during November 2007 (Bernardi et al., in preparation). The goals of this WSRT survey are to better understand the Galactic foregrounds, at frequencies in a range similar to that spanned by the LOFAR high-band antennas, and to test the calibration pipeline. The survey was carried during 6×12 h runs. One of the fields observed was the so-called Fan field (Bernardi, in preparation). Finally, we model the polarization leakage following Equation 13, with $d = 10^{-6}$ and $\psi = 0$. In this paper we ignore the radio-frequency interference (RFI) contamination and we assume that the data have been sufficiently corrected. We will consider the implications of insufficient RFI flagging and its effects on the signal extraction in the future.

Our final measurement equation, including all effects described above, can thus be written as:

$$\mathbf{A}(\nu, t) = \mathbf{G}(\nu, t) \mathbf{D}(\nu) \mathbf{E}(\nu, t) \mathbf{K}(\nu, t) \mathbf{F}(\nu, t) \mathbf{Z}(\nu, t) \quad (22)$$

with the parameters being defined as described in this section.

5.3.3 Additive Noise

Understanding the noise characteristics is very important for the LOFAR EoR-KSP, which aims to detect very weak radio emission. The noise properties of the instrument are vital for a sensible error analysis. The total effective collecting area for the LOFAR-EoR experiment is ~ 0.07 km² at 150 MHz. The instantaneous bandwidth of the LOFAR telescope is 32 MHz and the aim for the LOFAR-EoR experiment is to observe in the frequency range

between 115 and 180 MHz, which is twice the instantaneous bandwidth. To overcome this, multiplexing in time has to be used (for more details see, de Bruyn et. al 2007). For the purpose of this simulation we ignore this complication and assume 400 hours of integration time on a single field for a bandwidth of 32 MHz, centred at $\nu_0 = 150$ MHz. This is chosen for two reasons: first, the frequency of 150 MHz is the frequency where reionization presumably peaks in the current cosmological simulations. Second, due to the size of the data generated and the constraints of our current hardware (a 16-way symmetric multiprocessor system with 32 GB of memory), we are required to reduce the number of channels. This deteriorates the foreground fitting efficiency, but this is a reasonable compromise to be made. As we will show in the next section, this issue does not seem to pose any significant threat to our ability to statistically detect the EoR signal and our approach can thus be regarded as conservative.

The ultimate sensitivity of a receiving system is determined principally by the system noise. The noise properties of an elaborate receiving system like LOFAR can be very complex and we will address this more in forthcoming papers. The theoretical *rms* noise level in terms of the real and imaginary part of the complex visibilities for an interferometer pair between stations p and q is given by :

$$\Delta V \{\text{Re}, \text{Im}\}_{p,q} = \frac{1}{\eta_s} \times \sqrt{\frac{\text{SEFD}_p \times \text{SEFD}_q}{2 \times \Delta\nu \times \tau_{\text{avg}}}}$$

where η_s is the system efficiency that accounts for electronic, digital losses, $\Delta\nu$ is the frequency bandwidth and τ_{avg} is the averaging time during which each station accumulates data. SEFD is the System Equivalent Flux Density. The SEFD can be written as $\text{SEFD} = T_{\text{sys}}/K$, where $K = (\eta_a \times A_{\text{eff}})/(2 \times k_B)$ and depends on the station efficiency η_a and the effective collecting area A_{eff} of the station. k_B is the Boltzmann constant. For the system noise we assume two contributions. The first comes from the sky and is frequency dependent ($\approx \nu^{-2.55}$) and the second comes from the receivers. For the LOFAR HBA stations (24 tiles) the SEFD is ~ 2000 Jy at 150 MHz, depending on the final design (de Bruyn et. al 2007). We assume that the SEFD varies within one per cent between different stations. In order to calculate the SEFD we use the following system temperature (T_{sys}) scaling relation as function of frequency (ν):

$$T_{\text{sys}} = 140 + 60(\nu/300 \text{ MHz})^{-2.55}.$$

For our simulation, we scale the noise, so that in one night of observations we have the same sensitivity as the LOFAR-EoR observations after 400 hours. This is done because we currently lack the computational capacity to simulate and analyse a full data-cube of order several TBs per field. The equation above gives the noise on the real and imaginary parts of the visibility. When the SNR is high the noise distribution of the visibility amplitude and phase is Gaussian to an extremely good approximation. Without any signal the amplitude noise follows the Rayleigh distribution. When the SNR is low the measured amplitude noise follows the Rice distribution (Thompson, Moran, & Swenson 2001; Taylor, Carilli & Perley 1999; Lopez & Fabregas 2002) and gives a biased estimate of the true underlying signal. For the phases, the noise distribution becomes uniform.

In the following section we describe one method that demonstrates our ability to statistically detect the EoR signal from the post-calibration LOFAR maps that include realistic levels for the noise and zero-mean calibration residuals. In both cases for the statistical detection of the signal we use the total intensity maps only.

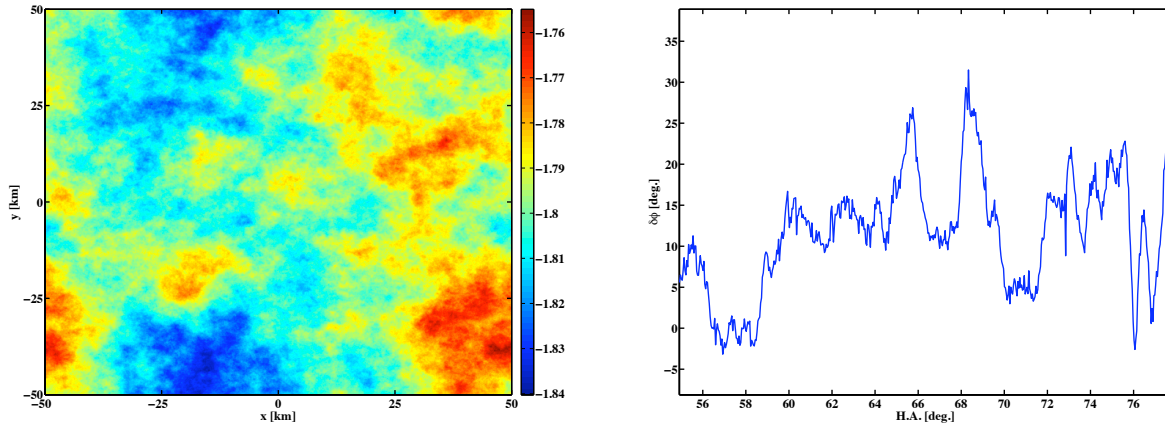


Figure 5. **Left:** A simulated map of the TEC of the ionosphere at a particular time, above the LOFAR core. Each LOFAR station sees approximately twenty square kilometers of the ionosphere at an altitude of 250 km. The values are displayed in TECUs. **Right:** Example of phase fluctuations caused by the ionosphere at a baseline of 100 metres as a function of Hour Angle

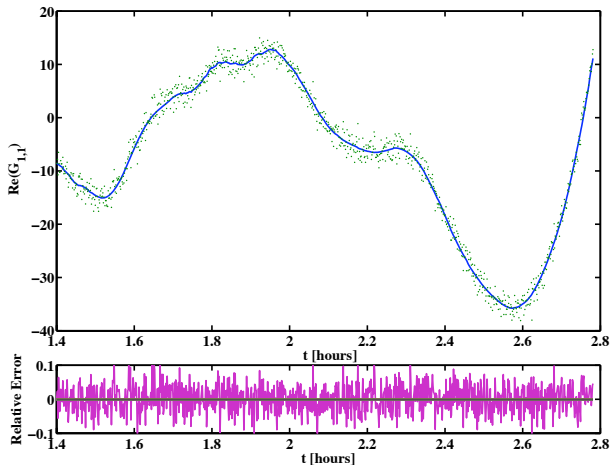


Figure 6. A plot of the real part of the complex gain for an XX correlation of a 500 m baseline at 150 MHz as function of time. The dots represent the recovered solution while the solid line the values used to corrupt the data. The relative error is plotted in the bottom panel.

In contrast to previous work, however, because we have taken polarization into account, its effects leaking into Q , U and V maps and are therefore accounted in our analysis. Gain calibration is assumed to be done with a precision of two per cent, which is a realistic estimate, judging from the experience gained thus far from the LOFAR Core Station One (CS1) data analysis.

5.4 The data–model inversion method

To invert the ME, we have rewritten it as a linear equation, relating the observed visibilities to the true underlying visibilities, using the properties of the outer Kronecker product (Golub & Loan 1989; Boonstra 2005). The relevant Jones–Mueller matrix describes the parameters of the model. This way we have to deal with a linear (over the parameters) model. Each parameter is a non-linear, multivariate function of other parameters that describe the physics behind each of the effects described by the relevant Jones matrices.

Due to our lack of information, though, we shall consider the elements of the Jones–Mueller matrix as multilinear functions of those parameters. Our task is to infer the parameters of the Jones–Mueller matrix, that we sample in the presence of Gaussian calibration errors and white noise.

The maximum-likelihood (ML) is a powerful method for finding the free parameters of the model to provide a good fit. The method was pioneered by R. A. Fisher (Fisher 1922). The maximum likelihood estimator (MLE) selects the parameter value which gives the observed data the largest possible probability density in the absence of a prior, although the latter can be easily incorporated. For small numbers of samples, the bias of maximum likelihood estimators can be substantial, but for fairly weak regularity conditions it can be considered asymptotically optimal (Mackay 2003). With large numbers of data points, such as in the case of the LOFAR EoR KSP, the bias of the method tends to zero. In general, it is not feasible to estimate the size of the data needed in order to obtain a good enough degree of approximation of the likelihood function to a multivariate Gaussian. We assume that errors associated with each datum are independent, but they have different variances and correlation properties over time and/or frequency. Many of these problems can be overcome by MCMC (Markov Chain Monte Carlo) or nested sampling of the posterior (Skilling 2004; Feroz, Hobson, & Bridges 2008).

Traditionally, the CLEAN/self-calibration approach has been used in radio-interferometry to give estimates of both the model parameters and the sky brightness distribution (Pearson & Readhead 1984). Given an initial model of the sky distribution, which is usually made using CLEAN components for a few bright sources with a known structure, we solve for the non-linear parameters \mathbf{p} of the model, and then improve the initial map. This is done in a loop until the optimization converges. In our approach, we make a distinction between the calibration and the data-model inversion parts. This is justified by the volume of the data to be handled. Another factor which is relevant for the EoR KSP is that we have to work near and below the noise level, and initial estimates of the sky distribution are going to be affected by the noise and calibration errors. We therefore need to make a proper determination of the true underlying visibilities and the model parameters, while retaining the noise and cosmological signal properties.

In our approach we assume that the parameter vector \mathbf{p} is

known within an accuracy of one to two per cent. For example, in Fig. 6, the gain used in the simulation and the recovered solution are shown. The parameter vector \mathbf{p} includes all the (non)-linear parameters of the instrumental and ionospheric models, that are part of the Jones matrices (see section 4.2). This is a key assumption and its impact needs to be determined. We will address this issue in the future, when the LOFAR roll-out will provide us with more data to test our current error estimation levels. Given that, the maximum likelihood solution can be formulated in a more powerful matrix formalism, as:

$$\left[\mathbf{M}_j^\dagger(\mathbf{p}) \mathbf{N}_{\text{noise}}^{-1} \mathbf{M}_i(\mathbf{p}) \right] \mathbf{b}_\nu = \left[\mathbf{M}_j^\dagger(\mathbf{p}) \mathbf{N}_{\text{noise}}^{-1} \right] \mathbf{v}_{\text{obs},\nu},$$

where $\mathbf{N}_{\text{noise}}$ is the determinable noise covariances and $\mathbf{M} = \mathbf{A} \otimes \mathbf{A}$. Its inverse plays the role of a metric in the N-dimensional vector space of the data. The metric is useful for answering questions having to do with the geometry of a vector space. In our case we use it to actually compute the dot product on that space. Solving this equation gives the ML solution for Gaussian noise. By linearizing the above ML equation along the eigenvectors of \mathbf{p} , we expect to find a better solution. Eventhough this can be done fully analytically, the complexity of the resulting matrices is so large that we plan to determine the later through forthcoming numerical simulations. By perturbing \mathbf{p} , we can then recover the proper noise and EoR covariance matrices and determine our final solution of \mathbf{s} . This process could even be iterated, but we expect convergence after a couple of iterations, since we start with an already good approximation of the model parameters. With the addition of extra regularization terms, a deconvolved image can be obtained, from which the foreground and point-sources can be subtracted or filtered, to leave only the EoR signal and the noise. This ‘ideal’ process, will be the subject of the second paper in this series. In the current paper, however, our main goal is to show that if calibration errors can be corrected without bias (i.e. errors on the correction have asymptotically zero mean), that we can indeed recover the EoR signal. Clearly, this is the first step in this process. In the following section we will therefore apply the more simple method used by Jelic et al. (2008), which does not do a ML inversion, but simply uses “dirty” images with identical synthesized beam shapes, in order to extract the cosmological signal from the dirty maps.

6 RESULTS FROM THE SIGNAL EXTRACTION

The ultimate benchmark whether we can, in principle, recover the redshifted 21-cm signal from the LOFAR EoR KSP data set, is to apply our ML inversion and our signal-recovery procedure to the simulated data with realistic sky, ionospheric and instrument settings, and if that is successful, ultimately to real data sets.

This, however, is not yet computationally feasible¹⁰ and we opt in this paper for a less computationally expensive approach by removing the foregrounds from the “dirty” images. We are in fact implementing the full ML method on a mini-cluster of three quad-core PCs connected to three NVIDIA Graphics Processor Units.

To remove the foregrounds, we currently use a polynomial fit along frequency for every line of sight on the “dirty” images. To produce the dirty maps we use only uv points that are present in 95% of the frequency channels (Figure 7). This leads to an identical PSF for every map, with the additional cost of resolution loss. The

¹⁰ Current tests indicate 30 hrs of computing time for the ML inversion of a single frequency channel of realistic data size on a single high-end CPU

Table 1. Values of the noise (σ_{noise} [mK] at 150 MHz), for different levels of calibration errors

	case (a)	case (b)	case (c)	case (d)
Error [%]	0.5	1	2	10
σ_{noise} [mK]	36	58	60	73

visibilities are gridded on a super-sampled, regular grid of 256 by 256 cells. This degrades the resolution of the dirty maps somewhat but minimizes any mixture between spatial and frequency fluctuations because of gaps in the uv-plane. Our current analysis is also done including only the Galactic foregrounds, and we will address the issue of the extragalactic foregrounds in the future, once we have more computational power available to us.

An inappropriate polynomial fitting, however, could remove part of the EoR signal or in the case of under fitting of the foregrounds, fitting residuals could dominate over the EoR signal (for details and discussion see Jelic et al. (2008)). Hence, after subtracting the foregrounds from the data cubes, the residuals should ideally contain only the noise plus the EoR signal. The noise level is nearly an order of magnitude larger than the EoR signal, however, so one is able to make only a statistical detection of the signal over the map by taking the difference between the variance of the residuals and the variance of the noise. The underlying assumption here is that the general statistical properties of the noise are known to a high accuracy as a function of frequency. We are currently investigating methods that provide accurate noise estimates from the or partly calibrated data.

Fig. 8 shows the standard deviation of residuals as a function of frequency (dashed line), after taking out the smooth component of the foregrounds using a third-order polynomial. The white dashed line represents the mean of the detected EoR signal after 100 independent Monte Carlo simulations of the extraction method applied to each realization, while the grey shaded zone shows 2σ detection limits. As one can see the detected EoR signal is in good agreement with the original (solid red line) for most the frequencies (Table 1). We use bold-face letters to mark our current expectations. We thus conclude that in this case we can still recover the EoR signal, while for larger errors we gradually lose our ability to statistically detect the EoR signal.

7 SUMMARY & OUTLOOK

The main goal of this paper has been to introduce a physics-based data model for the LOFAR EoR Key Science Project, use this data model to generate realistic data sets, including Galactic and extragalactic foregrounds and known instrumental, ionospheric and noise properties (with zero-mean residuals), and subsequently extract the redshifted 21-cm EoR signal from the data cubes. Despite simplifications, which we indicated and will further address in forthcoming papers, we have clearly made a large step forward in simulating *realistic* circumstances under which currently planned EoR experiments like LOFAR will operate. This has thus far been lacking in many publications on this topic, which have all neglected calibration and uv-sampling issues, and clearly needs to be addressed beyond overly simplified assumptions before results from any of the currently planned projects can be believed.

We have also shown that using the currently known or estimated instrument specifications and layout of LOFAR, the 21-cm EoR signal can be recovered if the noise properties are known a

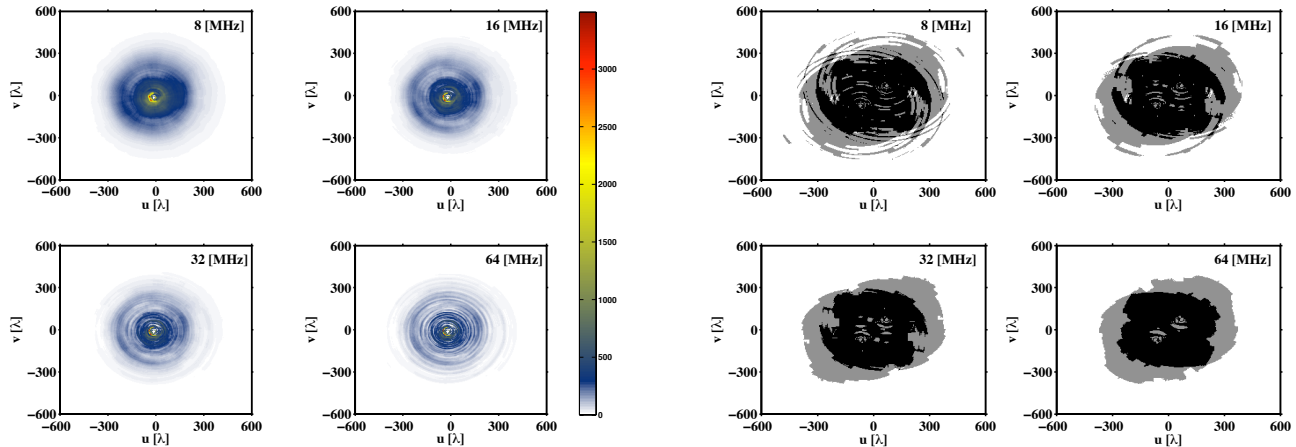


Figure 7. The sampling of the uv-plane by the LOFAR core along frequency after 6 hours of synthesis. The left-hand figures show the average number of visibilities per uv cell for 8, 16, 32 and 64 MHz of total bandwidth (the instantaneous bandwidth of LOFAR is 32MHz). We assume that the data are delivered at 0.1 MHz resolution. The colorbar shows the number of visibilities per grid point. The right-hand set of figures shows the area in which less than 5% of the data along frequency is lost due to the scaling of the uv coverage with frequency, compared to the the total bandwidth. The black points represent regions where the visibilities and their Fourier conjugates occupy the same place, while the grey points represent true visibility measurements. This distinction is made because the Fourier conjugates do not contribute to the SNR.

priori (although we have not yet tested whether the extraction of noise and EoR signal separately is possible), and the calibration of the ionosphere and instrument can be carried out in an unbiased fashion to the level that WSRT and LOFAR test setups indicate is possible. In forthcoming papers we will address far more complex situations that include all possible foregrounds (not only Galactic) and where calibration will be done using the simulated data themselves. This requires a considerable increase in our computational power and we are currently implementing our codes on GPUs to achieve the required processing power.

In more detail, in this paper we initially started by providing a brief description of the physical connections behind the Hamaker–Bregman–Sault formalism. This completes the picture established by Hamaker & Bregman (1996). The connection to physics helps in better understanding new and old problems in radio-polarimetry and provides a new perspective. Novel methods of calibration and image evaluation can be developed based on those principles and we indicated a few possibilities (see Appendix A).

After describing the connection between the physics of the Jones and Mueller calculi and the data model for a generic radio interferometric array, we introduced the data model that is relevant for the LOFAR EoR KSP. This description of the signal pathways was used to generate detailed, large-scale polarized instrumental response simulations for several instrumental parameters assuming simplified, but still realistic models for their values and errors. The high-resolution data produced by this simulation were generated in such a way that they resemble a typical LOFAR EoR observation.

We applied the same procedure, albeit simple, as described by Jelic et al. (2008) to recover the cosmological signal, and as a first benchmark of the inversion method. The polynomial fit method (Zaldarriaga, Furlanetto, & Hernquist 2004; Jelic et al. 2008) gives a reasonable result, even in the presence of small errors in the calibration parameters. When including realistic instrumental noise and calibration errors, we can still recover the cosmological signal if the properties of instrumental noise are well known as a function of frequency. In order to obtain the frequency dependence of the noise, we used the true underlying sky distribution. In reality,

one might not have this luxury. However, differencing of image or visibility values between narrow frequency channels could in principle deliver the noise properties of the instrument as function of frequency.

What has not been addressed in this paper, but will be in the follow-up paper, is the calibration process itself. The traditional self-calibration algorithm (Pearson & Readhead 1984) alternates between calibration and CLEAN steps in order to find the optimal image, from a given visibility data set. This is done by subtracting simple models for the sky brightness distribution and correcting for the calibration solutions at every step. This, however, leads to a sub-optimal solution and certainly cannot deal easily with complex sky brightness structures (Starck, Pantin, & Murtagh 2002; Bhatnagar & Cornwell 2004; Puetter & Piña 1994; Narayan & Nityananda 1986; Cornwell & Evans 1985; Kembal & Martinsek 2005). On the other hand, the maximum likelihood method has traditionally been used in many disciplines in order to estimate the parameters of linear systems. It can address the calibration, (after linearization), and deconvolution problems and in forthcoming papers we will further test this methodology, besides others [e.g. Expectation Maximization; Yatawatta et al. (2008)].

Finally, there is the problem of the signal extraction itself. Although done independently of the inversion process in this paper, we suspect it can possibly be done simultaneously with the inversion. This will also be addressed in forthcoming papers. Here, we have studied signal extraction through polynomial fitting, but matched filtering is another approach that we plan to take, and we suspect it might be a good complementary method. Those algorithms might have to make some use of a priori assumptions, though, since the observational evidence for the cosmological signal is scarce to non-existent.

A detailed analysis of the noise properties of the foreground-cleaned maps also still has to be carried out. This can be done in a Monte Carlo sense. This way one can study the asymptotic efficiency of the ML, using the observed information matrix. Another consideration should be the correlation properties between the in-

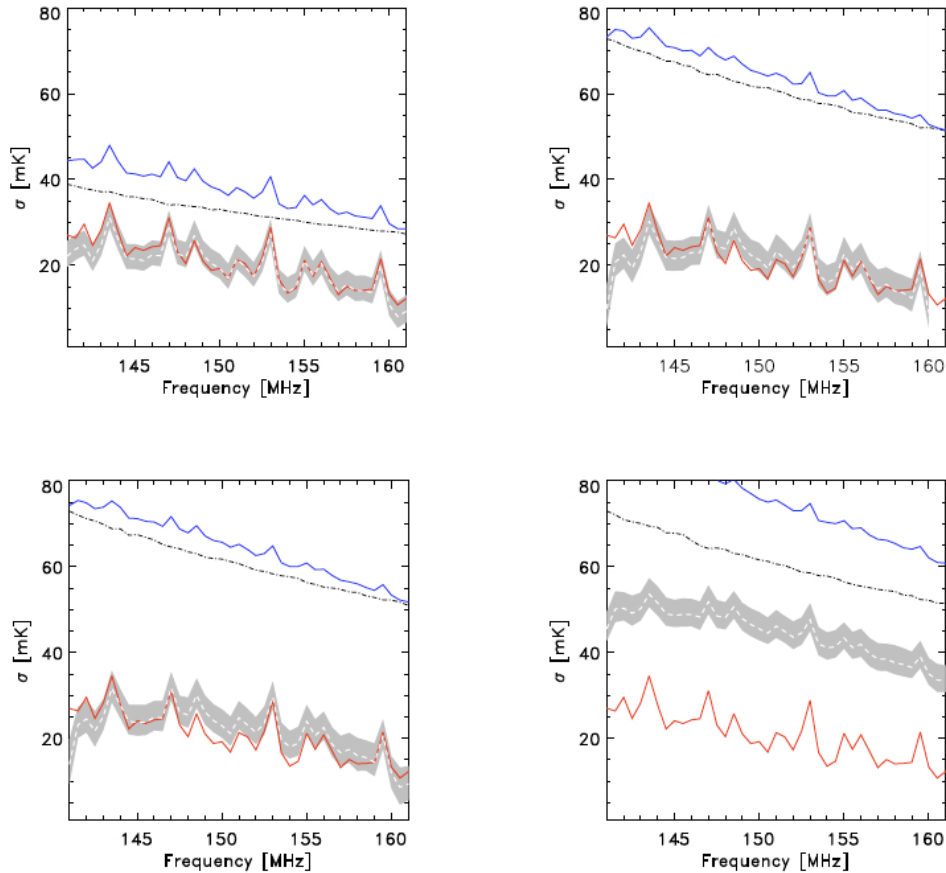


Figure 8. The signal extraction for (a) 0.5 per cent (top left), (b) 1 percent (top right), (c) 2 per cent (bottom left) and (d) 10 per cent (bottom right) errors on the calibration parameters. The solid blue line represents the *rms* value of the residuals of the fitting procedure. The black-dotted line is the *rms* of the instrumental noise as a function of frequency. The *rms* of the “dirty” map of the cosmological signal is plotted with the red line and of the extracted signal with the white dashed line. The shaded grey areas are the errors on the *rms* of the extracted signal calculated from 100 realizations of the noise. The effectiveness of the extraction procedure decreases rapidly with the amplitude of the errors.

strumental parameters, as well as the error propagation, since in principle their behaviour is highly non-linear.

Despite a considerable increase in the complexity of large-scale EoR simulations (Thomas et al. 2008), foregrounds models (Jelic et al. 2008) and the instrument model (this paper) – necessary to process and understand the results from our forthcoming LOFAR EoR KSP observations – with this paper we intend to provide a guide towards even more complex simulations, including all the effects that we mentioned above and thus far have avoided or implemented in a simplified manner. We conclude with the comment, learned from the current paper, that only by doing simulations and successful signal-recovery on a scale and complexity-level comparable to the real observations, can one convincingly show that ongoing experiments – be it LOFAR, MWA, or otherwise – are capable of extracting the redshifted 21-cm signal from data sets affected by noise, RFI, calibration errors and bright foregrounds. It is also essential in interpreting their ultimate results.

ACKNOWLEDGMENTS

The authors would like to thank Johan Hamaker, Jan Noordam, Oleg Smirnov and Stephan Wijnholds for useful discussions during the various stages of this work. LOFAR is being funded by the European Union, European Regional Development Fund, and by “Samenwerkingsverband Noord-Nederland”, EZ/KOMPAS.

REFERENCES

- Barakat R., 1963, *JOSA*, 53, 317
- Barkana R., Loeb A., 2001, *PhR*, 349, 125
- Becker R. H., et al., 2001, *AJ*, 122, 2850
- Berry M. V., 1987, *JMOp*, 34, 1401
- Bhatnagar S., Nityananda R., 2001, *A&A*, 375, 344
- Bhatnagar S., Cornwell T. J., 2004, *A&A*, 426, 747
- Bhatnagar S., Cornwell T. J., Golap K., Uson J. M., 2008, *A&A*, 487, 419
- Boonstra A.-J., 2005, *PhDT*,
- Born M., Wolf E., 1999, *poet.conf*,
- Bowman J. D., Morales M. F., Hewitt J. N., 2005, *AAS*, 37, 1217
- Bowman J. D., Morales M. F., Hewitt J. N., 2006, *ApJ*, 638, 20

- Bowman J. D., Morales M. F., Hewitt J. N., 2008, arXiv, arXiv:0807.3956
- Bregman J. D., 2002, IAUS, 199, 484
- Brentjens M. A., de f A. G., 2005, A&A, 441, 1217
- Bromm V., Larson R. B., 2004, ARA&A, 42, 79
- Brosseau C., *Fundamentals of polarized light: A statistical approach*, 1998, Wiley, N.Y.
- Burn B. J., 1966, MNRAS, 133, 67
- Carozzi T. D., Woan G., 2008, arXiv, arXiv:0812.0141
- Ciardi B., Ferrara A., White S. D. M., 2003, MNRAS, 344, L7
- Ciardi B., Madau P., 2003, ApJ, 596, 1
- Ciardi B., Stoehr F., White S. D. M., 2003, MNRAS, 343, 1101
- Cooray A., Furlanetto S. R., 2004, ApJ, 606, L5
- Cornwell T. J., Evans K. F., 1985, A&A, 143, 77
- de Bruyn G., Miley G., Rengelink R., et al., 1998, <http://www.strw.LeidenUniv.nl/wenss>
- de Bruyn G., Zaroubi S. & Koopmans L., 2007, LOFAR-EoR Project Plan
- Di Matteo T., Perna R., Abel T., Rees M. J., 2002, ApJ, 564, 576
- Di Matteo T., Ciardi B., Miniati F., 2004, MNRAS, 355, 1053
- Eliasson B., Thidé B., 2007, GeoRL, 34, 6106
- Eliasson B., Thidé B., 2008, JGRA, 113, 2313
- Falcke H. D., et al., 2007, HiA, 14, 386
- Fan X., et al., 2001, AJ, 122, 2833
- Fan X., et al., 2006, AJ, 132, 117
- Fano U., 1954, PhRv, 93, 121
- Fano U., 1957, RvMP, 29, 74
- Feretti L., 2002, IAUS, 199, 133
- Feroz F., Hobson M. P., Bridges M., 2008, arXiv, arXiv:0809.3437
- Field G. B., 1958, Proc. Inst. Radio Eng., 46, 240.
- Field G. B., 1959, ApJ, 129, 536
- Fisher, R., *Philosophical Transactions of the Royal Society, A*, 222:309-368 (1922)
- Fridman P. A., Baan W. A., 2001, A&A, 378, 327
- Furlanetto S. R., Oh S. P., Briggs F. H., 2006, PhR, 433, 181
- Gil J. J., 2007, EPJAP, 40, 1
- Gleser L., Nusser A., Benson A. J., 2007, arXiv, 712, arXiv:0712.0497
- Golub, G., Loan, C. V., *Matrix Computations - 2nd Edition*, Johns Hopkins University Press, Baltimore, Maryland, 1989.
- Green D. A., 1998, yCat, 7211, 0
- Gunn J. E., Peterson B. A., 1965, ApJ, 142, 1633
- Hamaker J. P., Bregman J. D., 1996, A&AS, 117, 161
- Hamaker J., 1999, NewAR, 43, 613
- Hamaker J. P., 2000, SPIE, 4015,
- Hamaker J., 2000, prat.conf, 323
- Hamaker J. P., 2000, A&AS, 143, 515
- Hamaker J. P., 2006, A&A, 456, 395
- Heiles C., et al., 2001, PASP, 113, 1274
- Heiles C., 2002, ASPC, 278, 131
- Hobson M. P., Maisinger K., 2002, MNRAS, 334, 569
- Hogan C. J., Rees M. J., 1979, MNRAS, 188, 791
- Högbom J. A., 1974, A&AS, 15, 417
- Iliev I. T., Pen U.-L., Bond J. R., Mellema G., Shapiro P. R., 2007, ApJ, 660, 933
- Jackson C., 2005, PASA, 22, 36
- Jelic V., et al., 2008, arXiv, 804, arXiv:0804.1130
- Jones R. C., 1941, JOSA, 31, 488
- Jones R. C., 1942, JOSA, 32, 486
- Jones R. C., 1948, JOSA, 38, 671
- Kemball A., Martinsek A., 2005, AJ, 129, 1760
- Kuhlen M., Madau P., 2005, MNRAS, 363, 1069
- Kumar A., Subramanian K., Padmanabhan T., 1995, JApAS, 16, 83
- Landi Degl'Innocenti E., 1987, nrt.book, 265
- Lay O. P., Halverson N. W., 2000, ApJ, 543, 787
- Leshem A., van der Veen A.-J., Boonstra A.-J., 2000, ApJS, 131, 355
- Leshem A., van der Veen A.-J., 2000, SPIE, 4015, 341
- Liu A., Tegmark M., Zaldarriaga M., 2008, arXiv, arXiv:0807.3952
- Loeb A., Barkana R., 2001, ARA&A, 39, 19
- Lopez, C.; Fabregas, X. *Electronics Letters Volume 38, Issue 20, 26 Sep 2002 Page(s): 1207 - 1208*
- Mackay D. J. C., 2003, itil.book
- Madau P., Meiksin A., Rees M. J., 1997, ApJ, 475, 429
- Manikas A., *Differential Geometry in Array Processing*, World Scientific Publishing Co Ltd, Imperial College Press. 2004
- Morales M. F., Bowman J. D., Hewitt J. N., 2005, AAS, 37, 1217
- Morales M. F., Matejek M., 2008, arXiv, arXiv:0810.5107
- Narayan R., Nityananda R., 1986, ARA&A, 24, 127
- Nijboer R. J., Noordam J. E., Yatawatta S. B., 2006, ASPC, 351, 291
- Noordam J. E., 1982, siha.conf, 257
- Noordam J. E., AIPS++ Implementation note 185
- Noordam J. E., 2000, SPIE, 4015, 366
- Noordam J. E., 2004, SPIE, 5489, 817
- Norin L., Grach S. M., Leyser T. B., Thidé B., Sergeev E. N., Berlin M., 2008, JGRA, 113, 9314
- Nusser A., 2005, MNRAS, 359, 183
- Oh S. P., Mack K. J., 2003, MNRAS, 346, 871
- Pacholczyk A. G., 1970, ranp.book,
- Page L., et al., 2007, ApJS, 170, 335
- Parke N. G., III, 1948, PhDT
- Pearson T. J., Readhead A. C. S., 1984, ARA&A, 22, 97
- Pen U.-L., Chang T.-C., Peterson J. B., Roy J., Gupta Y., Hirata C. M., Odegova J., Sigurdson K., 2008, arXiv, arXiv:0807.1056
- Pentericci L., et al., 2002, AJ, 123, 2151
- Platania P., Bensadoun M., Bersanelli M., de Amici G., Kogut A., Levin S., Maino D., Smoot G. F., 1998, ApJ, 505, 473
- Puetter R., Piña R. K., 1994, shsr.conf, 61
- Reich P., Reich W., 1988, A&AS, 74, 7
- Reich W., 2006, astro, arXiv:astro-ph/0603465
- Reid R. I., Gray A. D., Landecker T. L., Willis A. G., 2008, RaSc, 43, 2008
- Reimer M. and Yevick D., *Photonics Technology Letters, IEEE Volume 18, Issue 6, March 15, 2006 Page(s):734 - 736 doi: 10.1109/LPT.2006.871134*
- Rogers A. E. E., Bowman J. D., 2008, AJ, 136, 641
- Santos M. G., Cooray A., Knox L., 2005, ApJ, 625, 575
- Sault R. J., Hamaker J. P., Bregman J. D., 1996, A&AS, 117, 149
- Schwarz U. J., 1978, A&A, 65, 345
- Scott D., Rees M. J., 1990, MNRAS, 247, 510
- Shaver P. A., Windhorst R. A., Madau P., de Bruyn A. G., 1999, A&A, 345, 380
- Skilling J., 2004, AIPC, 735, 395
- Smirnov O. M., Noordam J. E., 2004, ASPC, 314, 18
- Smirnov O. M., Noordam J. E., 2006, ASPC, 351, 355
- Smoot G. F., 1998, astro, arXiv:astro-ph/9801121
- Spergel D. N., et al., 2007, ApJS, 170, 377
- Spoelstra T. A. T., Schilizzi R. T., 1981, seus.proc, 315
- Spoelstra T. A. T., Yang Y.-P., 1990, ursi.symp, 189
- Spoelstra T. A. T., 1995, JATP, 57, 163
- Spoelstra T. A. T., 1996, JATP, 58, 1229

Springel V., 2005, MNRAS, 364, 1105
 Starck J. L., Pantin E., Murtagh F., 2002, PASP, 114, 1051
 Sunyaev R. A., Zeldovich I. B., 1975, MNRAS, 171, 375
 G. B. Taylor, C. L. Carilli, R. A. Perley, 1999, rpa..book
 Thidé B., 2007, PPCF, 49, 103
 Thomas R. M., Zaroubi S., 2008, MNRAS, 384, 1080
 Thompson A. R., Moran J. M., Swenson G. W., Jr., 2001, isra.book,
 Tinbergen J., 1996, aspo.book,
 van der Tol, S.; van der Veen, A.-J., "Ionospheric Calibration for the LOFAR Radio Telescope," Signals, Circuits and Systems, 2007. ISSCS 2007. International Symposium on , vol.2, no., pp.1-4, 13-14 July 2007
 van Trees H., Optimum Array Processing (Detection, Estimation, and Modulation Theory, Part IV) , 2002, isra.book
 van Velthoven P. F. J., Spoelstra T. A. T., 1992, AdSpR, 12, 211
 Veen A. J., Leshem A., Boonstra A. J., 2004, ExA, 17, 231
 Veen A. J., Leshem A., Boonstra A. J., 2004, ExA, 17, 231
 White R. L., Becker R. H., Fan X., Strauss M. A., 2003, AJ, 126, 1
 Wild J. P., 1952, ApJ, 115, 206
 Wijnholds S. J., Bregman J. D., Boonstra A. J., 2004, ExA, 17, 35
 Wouthuysen S. A., 1952, AJ, 57, 31
 Yatawatta S., Zaroubi S., de Bruyn G., Koopmans L., Noordam J., 2008, arXiv, arXiv:0810.5751
 Zaldarriaga M., Furlanetto S. R., Hernquist L., 2004, ApJ, 608, 622
 Zaroubi S., Silk J., 2005, MNRAS, 360, L64
 Zaroubi S., Thomas R. M., Sugiyama N., Silk J., 2007, MNRAS, 375, 1269

APPENDIX A: PROPERTIES OF THE STOKES VECTOR AND MATRIX

In this appendix we introduce several fundamental concepts in the description of polarized radiation. Although not yet used in this paper, we feel that they are important to mention and will be used in forthcoming publications to guide us to a better understanding of complex calibration processes in radio interferometry.

A1 Pauli Matrices

Pauli matrices are well known and have been used for the analysis of partially polarized light (Fano 1954). Their major advantage is that they satisfy a set of properties that significantly reduce the complexity of calculations associated with the intensity. The identity plus the Pauli matrices in two dimensions are defined as

$$\begin{aligned} \sigma_0 &= \begin{pmatrix} 1 & 0 \\ 0 & 1 \end{pmatrix} & \sigma_1 &= \begin{pmatrix} 1 & 0 \\ 0 & -1 \end{pmatrix} \\ \sigma_2 &= \begin{pmatrix} 0 & 1 \\ 1 & 0 \end{pmatrix} & \sigma_3 &= \begin{pmatrix} 0 & -i \\ i & 0 \end{pmatrix} \end{aligned} \quad (\text{A1})$$

This set of 2×2 linearly independent matrices constitute a basis for the vector space of 2×2 Hermitian matrices over the complex numbers. Summarizing their properties, they are Hermitian and they follow the commutation relations $[\sigma_i, \sigma_j] = \sigma_i \sigma_j - \sigma_j \sigma_i = i2\varepsilon_{ijk} \sigma_k$ where ε_{ijk} is the Levi-Civita permutation symbol (Golub

& Loan 1989; Fano 1954; Boonstra 2005). These matrices are unitary and traceless except for the identity matrix. The linear expansion of the coherency matrix in this basis is

$$\mathbf{C} = \frac{1}{2} \sum \text{tr}(\mathbf{C}\sigma_i)\sigma_i \quad (\text{A2})$$

with $s_i = \text{tr}(\mathbf{C}\sigma_i)$ being the four Stokes parameters: $i = 0, 1, 2, 3$ corresponding to the Stokes I, Q, U and V , respectively.

A2 The Stokes Vector and Matrix

In the literature the Stokes parameters are usually arranged as a 4×1 vector, $\mathbf{s} = (I, Q, U, V)^T$ (Gil 2007). An alternative notation would be to introduce a 2×2 Stokes matrix.

$$\mathbf{S} = \frac{1}{2} \begin{pmatrix} I + Q & U - iV \\ U + iV & I - Q \end{pmatrix} \quad (\text{A3})$$

In this case for pure states we have $\|\mathbf{C}\|^2 = \frac{1}{2} \|\mathbf{S}\|^2$ and in the case of unpolarized light $\|\mathbf{C}\|^2 = \frac{1}{4} \|\mathbf{S}\|^2$. This is because for unpolarized light Q, U and V are zero and the matrix becomes I multiplied by the identity matrix. Since there is a factor of $\frac{1}{2}$, the Frobenius norm of the matrix has this factor squared. Even if the source is not polarized one should observe the same signal in both orthogonal polarizations, as in this case both polarization states are equiprobable. This is an important fact for calibration. The X and Y dipoles of the LOFAR HBAs should measure the same signal, for unpolarized sources, and any fluctuations should be due to polarization calibration errors.

A3 Polarization Level

In addition, the degree of polarization is defined as $P \equiv \sqrt{U^2 + V^2 + Q^2}/I$. We can also define the unit vector (Gil 2007)

$$\mathbf{p}^T = \frac{1}{PI} \begin{pmatrix} Q \\ U \\ V \end{pmatrix}$$

The Stokes vector can be decomposed using those parameters in several ways. A trivial decomposition is between a polarized and unpolarized state. As radio receivers are intrinsically polarized, and in the case of LOFAR orthogonal, a spectral decomposition can express the Stokes vector as a convex linear sum of two orthogonal pure states. This makes the relationship between the measured signals and the parameters describing the system more clear, since we have to deal with orthogonal states. The spectral decomposition of the coherency matrix is using its eigenvalue structure to decompose it into pure states, i.e. eigenvectors. The spectral decomposition (diagonalization) of the coherency matrix is then equivalent to

$$\mathbf{s} = I \times \left(\frac{1+P}{2} \begin{bmatrix} 1 \\ \mathbf{p}^T \end{bmatrix} + \frac{1-P}{2} \begin{bmatrix} 1 \\ -\mathbf{p}^T \end{bmatrix} \right)$$

Of course, for a mixed state there are infinite combinations of independent states into which it can be decomposed, but it would be useful if the selection is such that it matches the characteristics of the system. The parameters I and P are invariant under unitary transformations (changes of coordinate systems). They are directly related to the eigenvalues of \mathbf{C} . Pure states are related to rank-1 polarization matrices, and mixed states to rank-2. Wolf showed that there always exist two orthogonal reference directions, such that the degree of coherence is maximized and coincides with P . This is important because various random distributions correspond to unpolarized light. The measurement of the correlations of the Stokes

parameters allows us to distinguish between those different types of non-polarized light.

A4 Entropy

Concluding with the quality criteria, the von Neumann entropy can be applied to electromagnetic waves (Fano 1957; Brosseau 1998). In terms of the coherency matrix it is defined as $S = -\text{tr}(\hat{\mathbf{C}} \ln \hat{\mathbf{C}})$. Is a measure of the difference in the amount of information between pure and mixed states, both with same intensity. It can be expressed as a function of the eigenvalues of \mathbf{C} as $S = -\frac{1}{2} [(1+P) \ln(\sqrt{1+P}) + (1-P) \ln(\sqrt{1-P})]$. It is a decreasing monotonic, bounded function of P (Gil 2007). It attains its maximum value, $S = \ln(2)$, for non polarized light and its minimum, $S = 0$, for totally polarized light. Using this entropy one can define the polarization temperature. Depolarizing effects, such as the ionospheric Faraday rotation, can be studied this way in order to detect spatial heterogeneity. For example, ionospheric TIDs should lead to an increase in the polarization entropy. This is a good scheme of ranking observations: if the polarization entropy differs between two maps, residual Faraday rotation and leakage can be present. Finally, for non-Gaussian distributions of polarization states, higher order moments are needed and the Stokes system is no longer adequate to describe the polarization states.

The standard (self)-calibration procedure for interferometric observation of polarized light aims at recovering the coherency matrix of the polarized radiation. Given the statistical nature of the coherency matrix, we must emphasize the importance of parameters that give a measurement of their polarimetric purity. Polarization entropy is a concept related to the impurities of the media through which radiation propagates, as it was defined above. It is useful for many purposes, especially when depolarization is a relevant subject. An increase in the polarization entropy signifies a decrease in the polarization purity. It is a direct way to access the quality of the data. Ionospheric Faraday rotation causes a depolarization with a certain frequency behavior. We would expect that the entropy would follow this behavior. In Figure A1 we show the polarization entropy for several lines of sight as a function of frequency in a simulated map. Attention should be brought to the fact that is really hard to distinguish between Faraday rotation and other depolarization effects.

A5 Lorentz Transformations

The transformations of the Stokes vector lead to a system of differential equations (Landi Degl’Innocenti 1987). From the statistical interpretation of the coherency matrix we derive that the Stokes I parameter has to be positive and that $s_0 = I \geq s_1^2 + s_2^2 + s_3^2 = Q^2 + U^2 + V^2$, which means that there can be no more polarized light than the total light. This is a key concept in physics, namely the conservation of energy. Extending this remark, we can define a Minkowski space (in the mathematical sense) for the Stokes 4-vectors. The norm in this space would be $\|\mathbf{s}\| = I^2 - Q^2 - U^2 - V^2$. Positive values of the norm correspond to the time-like vectors of the special theory of relativity. Light-like Stokes vectors correspond to totally polarized states. The Poincare sphere defines the light cone with the exception that the symmetric part of the cone does not have any special meaning. The Jones vector transforms as usual under the Lorentz group. The coherency matrix is defined through the Kronecker product of two Jones vectors and is a 2×2 spinor of rank two. The Stokes vector and the coherency matrix must be

realizations of the same irreducible representation of the Lorentz group, as they both have 4 independent components. The Lorentz transformations form a 6 parameter group. The six generators are the 3 spatial rotation generators of $O(3)$ \mathbf{R} and the Lorentz boosts \mathbf{B} . The infinitesimal transformation of the Stokes vector is

$$\mathbf{s}' = \mathbf{s} - \sum_i^3 (r_i \mathbf{R}_i + b_i \mathbf{B}_i) \mathbf{s} dI = \mathbf{s} - \mathbf{K} \mathbf{s} dI$$

where \mathbf{K} is a matrix that resembles the absorption matrix. This equation is the radiative transfer equation along the signal path. If one choses to exclude effects that intensify the radiation, this is the complete mathematical description of the effects in the signal path. The Lorentz boosts describe polarizing effects, while the spatial rotations describe the Faraday rotation. The relation between the initial and final Stokes vector is a finite Lorentz transformation. While it sounds straightforward it is not an easy task. The problem arises from the non commutativity of the generators. Magnus has proposed a solution to this problem. We will discuss this soon.

A6 Clifford Algebra

After having introduced the coherency matrix and the Jones formalism we proceed a step further in the mathematical abstraction in order to unify all possible cases. We note that every system is equivalent to a parallel combination of pure systems, and any pure system to a combination of retarders and diattenuators. In Hamaker (2000c) the author proposes the use of the quaternion algebra to describe the Jones matrices, or their $SO^+(1, 3)$ covering group. Quaternions, as any other space isomorphic to \mathbb{C} constitute a sub-algebra of a Clifford algebra. In particular, in three dimensions the Clifford product is equivalent to spatial rotations. Pure systems can still be described as Lorentz transformations in this algebra. Since algebraic manipulations become more clear, the computational requirements of problems involving partial polarization can be reduced. The Clifford algebra of three-dimensional space Cl_3 represents the four dimensional Minkowski space time. Clifford algebras have been used extensively to describe polarization mode dispersion (PMD) in optical fibres (Reimer & Yevich 2006). In that field they have to deal with a spatially inhomogeneous, birefringent medium (the optical fibre), which resembles the effects caused by the ionosphere on the EM waves that propagate through it.

A7 Magnus Expansion

In the case of polarization mode dispersion, which can occur due to ionospheric Faraday rotation, transversal of the polarized source signal through a set of phase screens etc, one is interested in recovering the original polarization state of the radiation. Two possibly quasi-orthogonal modes, represented by the input frequency-independent and the output Jones vectors, are related through a complex 2×2 Jones matrix. Despite the fact that we might not have any prior knowledge about the structure of the medium through which radiation propagates, the frequency dependence of that effect contains useful information about that medium. For example the $\sim \lambda^2$ Faraday rotation should leave a distinct imprint on the signal, which can help us distinguish it from other depolarizing effects. In the general case, the coherency matrix is transformed as $\mathbf{C}' = \mathbf{J} \mathbf{C} \mathbf{J}^\dagger$. An arbitrary Jones matrix with determinant 1, can be also expressed in terms of two vectors \mathbf{a} and \mathbf{b} according to

$$\mathbf{J} = \exp[-(i/2)(\mathbf{b} + i\mathbf{a}) \cdot \boldsymbol{\sigma}], \quad (\text{A4})$$

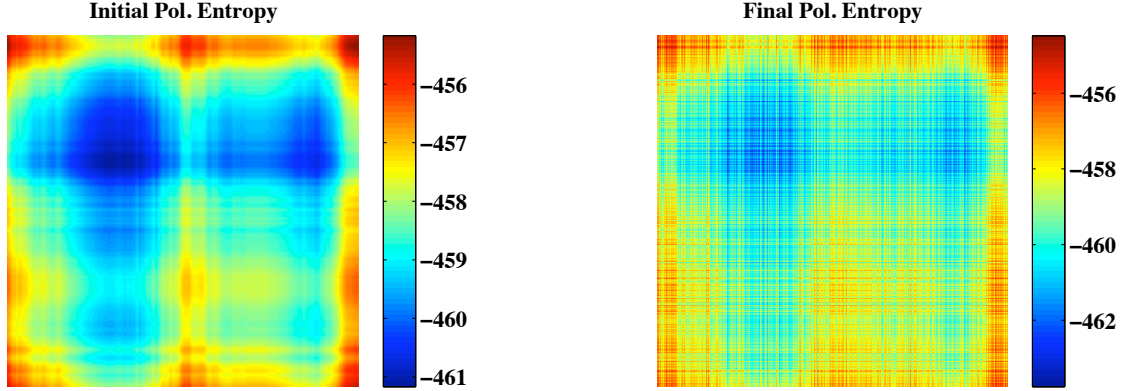


Figure A1. Left: the polarization entropy of a simulated Galactic diffuse synchrotron emission map. Right: the same plot after applying a depolarizing effect (Faraday rotation) along the horizontal axis

where σ is the Pauli spin vector. This is a Jones matrix representation of the Lorentz transformation in a Clifford algebra. In the case of a frequency dependent effect, $\mathbf{J}(\omega)$, the Jones space operator can be decomposed into real and imaginary components as

$$\begin{aligned} \mathbf{J}(\omega) &= \exp[-(i/2)(\mathbf{b} + i\mathbf{a}) \cdot \sigma], \\ \tilde{\mathbf{J}}_\omega \tilde{\mathbf{J}} &= -\frac{i}{2}[\boldsymbol{\Omega} + i\mathbf{A}], \end{aligned} \quad (\text{A5})$$

where the subscript ω represents differentiation with respect to the frequency. A solution for \mathbf{J} can be obtained through the Magnus expansion, which specifies $\mathbf{J}(\omega) = \exp\left(\sum_{n=0}^{\infty} \mathbf{B}_n(\omega)\right) \mathbf{J}(\omega_0)$, where the first two coefficients are given by

$$\begin{aligned} \mathbf{B}_1(\omega) &= \int_{\omega_0}^{\omega} d\omega_1 J_\omega(\omega_1), \\ \mathbf{B}_2(\omega) &= \int_{\omega_0}^{\omega} \int_{\omega_0}^{\omega_1} d\omega_2 d\omega_1 (J_\omega(\omega_1) J_\omega(\omega_2) - J_\omega(\omega_2) J_\omega(\omega_1)). \end{aligned}$$

The coefficients of the Magnus expansion for $n > 2$, are related to those of lower order through recursion. Taylor expanding the frequency derivatives of the Jones matrix to third order gives us a way to directly evaluate the Magnus coefficients. To the extent of our knowledge, the methods mentioned above have not been applied in the field of radio interferometry.